

UC San Diego

UC San Diego Electronic Theses and Dissertations

Title

Dynamic behavior and Martensitic transformation of FeNiCoAlTaB high entropy alloy

Permalink

<https://escholarship.org/uc/item/9c69635v>

Author

Huang, Aomin

Publication Date

2020

Peer reviewed|Thesis/dissertation

UNIVERSITY OF CALIFORNIA SAN DIEGO

Dynamic behavior and Martensitic transformation of
FeNiCoAlTaB high entropy alloy

A Thesis submitted in partial satisfaction of the requirements for the degree
Master of Science

in

Materials Science and Engineering

by

Aomin Huang

Committee in charge:

Professor Marc Meyers, Chair
Professor Shengqiang Cai
Professor Javier Garay

2020

Copyright
Aomin Huang, 2020
All rights reserved.

The Thesis of Aomin Huang is approved and it is acceptable in quality and form for publication on microfilm and electronically:

Chair

University of California San Diego
2020

Table of Contents

Signature Page	iii
Table of Contents	iv
List of Figures	vii
List of Tables.....	x
Acknowledgements.....	xi
Abstract of the Thesis	xii
1. Introduction.....	1
1.1 Multicomponent alloys	1
1.2 High entropy alloys.....	1
1.2.1 Core mechanism of HEA	2
1.2.1.1 Lattice distortion	2
1.2.1.2 Sluggish diffusion effect	3
1.2.1.3 High entropy effect	3
1.2.1.4 Cocktail effect.....	4
1.3 Deformation induced Martensitic transformation.....	5
1.4 Addition of element	8
1.5 Precipitates in NCATB.....	9
1.6 Strain rate effect.....	10
1.7 Shear localization.....	10
1.8 Microband.....	11

1.9	Scanning transmission electron microscope	13
2.	Experiment and method	13
2.1	Synthesis method	13
2.2	Microstructure analysis	14
2.2.1	XRD	14
2.2.2	EBSD	14
2.3	Quasi-static & Dynamic compression test	14
2.3.1	Quasi-static compression test.....	15
2.3.2	Dynamic compression test	16
2.4	Chemical composition analysis using EDX.....	21
2.5	Lamella lift out.....	21
2.6	Etching and polishing	22
2.7	Scanning transmission electron microscope	23
3.	Mechanical behavior and microstructure	23
3.1	Hall-Petch strengthening.....	23
3.2	Strain hardening and shear localization	26
3.3	Solid solution strengthening	34
3.4	Strain rate effect.....	41
3.5	Martensitic transformation.....	42
3.5.1	Strain rate effect on martensitic transformation.....	47
3.5.2	Morphology of deformation induced martensite	51
3.5.3	Nucleation of α' martensite.....	56

3.5.4 Grain size effect on martensitic transformation.....	60
3.6 Failure under quasi-static compression test	60
3.7 β -NiAl Grain boundary precipitates	63
3.8 Microband	65
4. Conclusion	70
5. Future work.....	72
6. References.....	73

List of Figures

Figure 1.1 Phase diagram of ternary and quaternary system.	1
Figure 1.2 lattice distortion in HEAs.	3
Figure 1.3 (a)Influence of number of equimolar elements on the mixing entropy of the system ^[27]	4
Figure 1.4 Schematic illustration of stress induced martensitic transformation.	8
Figure 1.5 Schematic of Cottrel-Lomer lock (interaction between two partial dislocation).	12
Figure 2.1 Instron quasi compressor.	15
Figure 2.2 Split Hopkinson pressure bar.	17
Figure 2.3. Dimension of hat shape specimen for dynamic test.	19
Figure 2.4 Configuration of shear strain area in hat shape specimen.	20
Figure 2.5 Ion beam cutting and thinning.	22
Figure 3.1 SEM image of undeformed NCATB.	26
Figure 3.2 Stress strain curves for (a) Dynamic compression test (b) Quasi-static compression test.	27
Figure 3.3 Shear stress strain curve.	30

Figure 3.4 $\log(\tau - \tau_0)$ vs. $\log \gamma$ and their fitting line.....	31
Figure 3.5 SEM image (a,b,c) of shear band.	33
Figure 3.6 (a) STEM HAADF image shows planar dislocation slips and multiple dislocation half-loops. (b) Coherent L_{12} phases (in the red circle areas). (c) FFT (fast Fourier transformation) pattern (in the yellow box) confirms the FCC matrix structure and L_{12} precipitation structure in the [001] zone axis.	39
Figure 3.7 XRD result of NCATB HEA before mechanical test.	40
Figure 3.8 XRD patterns of NCATB HEA with different grain size ($136 \mu m$ and $182 \mu m$) ^[48]	40
Figure 3.9 $\ln(\sigma - \sigma_0)$ vs. $\ln \epsilon$	42
Figure 3.10 Heating and cooling procedure of NCATB aged under $600^\circ C$ and $700^\circ C$ with M_s and A_f marked ^[52]	44
Figure 3.11 EDX configuration of undeformed NCATB materials.	46
Figure 3.12 Temperature rise vs. strain ^[19]	48
Figure 3.13 Kinetic parameter $\alpha \& \beta$ vs. Temperature reported by Cohen ^[47]	49
Figure 3.14 Mixture of FCC matrix and deformation induced martensite.	53
Figure 3.15 EBSD band contrast (BC) map.....	54
Figure 3.16 EBSD BC map (a & a') and EBSD IPFX map (b & b') of deformation induced martensite with different orientation.	55

Figure 3.17 Configuration of martensite morphology under different aging time (700°C).....	56
Figure 3.18 (a)(b) HRTEM BF (bright field) images of high strain rate deformed NCATB specimen (c) FFT pattern in selected area (red box)	59
Figure 3.19 EDX mapping for cracking area. Element distribution of: (a)Al (b)Fe (c)Co (d)Ni (e)Ta	61
Figure 3.20 EDX mapping for cracking area. Element distribution of: (a)Al (b)Fe (c)Co (d)Ni (e)Ta	62
Figure 3.21 Image of triple point junction grain boundary.....	64
Figure 3.22 Grain boundary precipitates in deformed hat shape specimen after etching.....	65
Figure 3.23 Configuration of formation of Ta and NiAl- β precipitates at grain boundaries, Pink line is high-angle boundaries ($>15^\circ$), blue line is low angle boundary ($<15^\circ$) ^[55]	65
Figure 3.23 SEM image of microband.....	67
Figure 3.24 IPFY images and its corresponding misorientation profile of microband	67
Figure 3.25 (a) EBSD phase map of microbands (b) IPFZ (inverse pole figure) map of microband	68
Figure 3.26 EBSD phase map of microband(green) and surrounding martensite(yellow)	69

List of Tables

Table 2.1 Purity of various raw materials for arc melting synthesis.....	13
Table 2.2 Dimension of specimen for quasi-compression test.	16
Table 2.3 Dimension of cylindrical specimen for dynamic compression test	19
Table 3.1. Mechanical data for quasi-static compression.	28
Table 3.2 Average precipitate size of γ' at aging temperature of 600°C and 700°C....	37
Table 3.3 Morphology of martensite and their corresponding M_s temperature and substructure.	52

Acknowledgements

I would like to acknowledge Prof. Marc Meyers' support and guidance throughout my researches and work on my master thesis for last two years and also his support for being my committee chair.

I would also like to show my gratefulness to Dr. Chen Zhang from UCI for his effort of providing FeNiCoAlTaB high entropy specimen through arc melting and performing high resolution transmission electron microscope and electron back scatter diffraction analysis.

I also like to thank Dr. Zezhou Li for helping me throughout my researches.

I would like thank Prof. Cai and Prof. Garay for attending and being my committee members and their valuable advices.

I would like to show my gratefulness to Dr. Zezhou Li for his valuable advices on my thesis and researches.

ABSTRACT OF THE THESIS

Dynamic behavior and Martensitic transformation of
FeNiCoAlTaB high entropy alloy

by

Aomin Huang

Master of Science in Materials Science and Engineering

University of California San Diego, 2020

Professor Marc Meyers, Chair

Owing to superior mechanical properties such as high fatigue life and high yield strength of many non-equiatomic high entropy alloys (HEA), a novel division of non-equiatomic FeNiCoAlTaB (NCATB) HEAs has been introduced. The novel NCTAB HEAs exhibit a very high yield stress which is around 1.1~1.2 GPa with appreciable ductility under quasi-static compression. The strengthening mechanisms in NCATB-HEA system are strongly dependent on the grain precipitates, solid solution and martensite transformation under dynamic loading. Martensitic transformation can commonly be attributed to athermal induction and deformation induction. In respect of athermal induced martensitic transformation, temperature of bulk materials needs to be lowered below M_s temperature rapidly. Whereas,

martensitic transformation can commence above M_s temperature. The chemical driving force for phase transition can be balanced through drastic cooling or external loading. Different shape of martensite (lath, butterfly, lenticular, thin plate) can be formed depending on the temperature while the lath-like martensite tends to appear at highest forming temperature and thin plate tends to appear at lowest forming temperature. Due to its superior mechanical properties including higher strength and strain hardening rate and high endurance limit, this novel HEA system is considered to be conducted into wider application including high damping materials and aviation application. The strain rate effect on martensitic transformation is also studied in current research. Microband is a very common phenomenon in high stacking fault energy material, whereas its formation mechanism remains unclear. Microband formation and its effect on martensitic transformation are also dedicated to study in this research.

1. Introduction

1.1 Multicomponent alloys

Traditional thought of researches on novel materials mainly obeys rules with combination of specific properties coming from different component. The mean goal of developing multicomponent alloys is to achieve balance of engineering properties attributed to different components. Conventional alloying strategies of one or two components materials were first discovered by Cantor^[25]. Besides, materials with several components (three or four) can be described through ternary and quaternary phase diagram^[27].

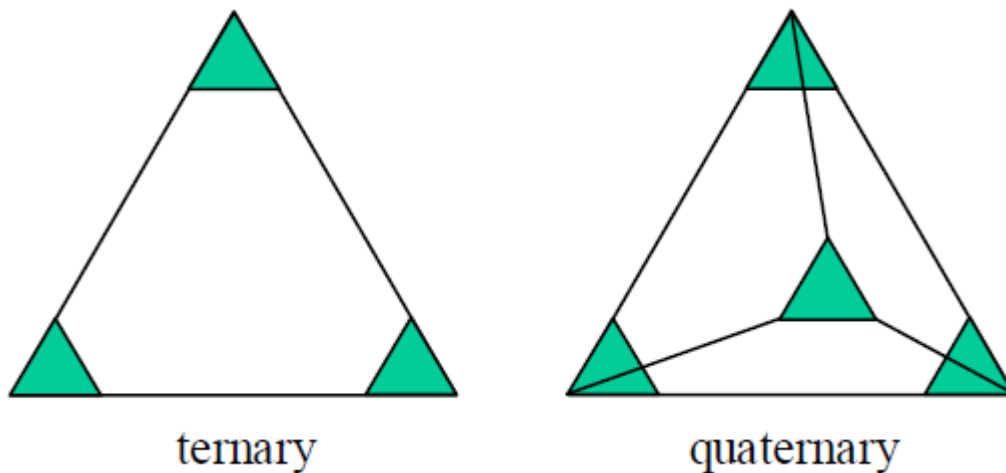


Figure 1.1 Phase diagram of ternary and quaternary system^[27].

1.2 High entropy alloys

High-entropy alloys, which are regarded as alloys consisting of five or more elements equally or near equally, were first discovered back in 1980s. Related theories were further developed by Jien-Wei Yeh in 1990s. The very first fabricated HEA alloy is CrMnFeCoNi alloy, which is also known as “Cantor” alloy. Upon the

previous researches, many other high-performance alloys tend to form intermetallic compounds which are undesired in terms of mechanical properties due to its negative influence of distribution of phases such as low stability based on Gibbs phase rule. Base on Gibbs phase rule, the increasing of instability of the system is corresponding to the growing number of phases. The equiatomic HEAs have been extensively investigated, therefore, more and more emphasis has been put on the study of non-equiatomic HEAs. The HEAs are mainly divided into two divisions in respect of different matrix phase, composed of BCC and FCC. Significantly more researches have been done on FCC-based HEAs than BCC-based HEAs. Besides many high entropy alloys possess strong temperature dependence mechanical behavior. For instance, the FCC Cantor alloy exhibits an increasing yield strength as temperature decreases at ranges between 77 to 500K^[8]. In contrast to FCC-based HEAs, much less information and details was obtained for BCC-based HEAs.

1.2.1 Core mechanism of HEA

1.2.1.1 Lattice distortion

Regularly, atoms should be periodically presenting in a unit cell, in other word, certain atom will locate at specific sites. Whereas, in some special cases, atoms may present at some unexpected sites. In multiple component alloys, distinct atomic size can generate strain and strain energy. The extent of lattice distortion is closely related to atomic radius difference and Poisson's ratio ν of materials. In terms of characterization, lattice distortion effect will weaken intensity peaks in

XRD due to smaller value of structure factor F. In other aspect of properties, the solid solution hardening is enhanced.

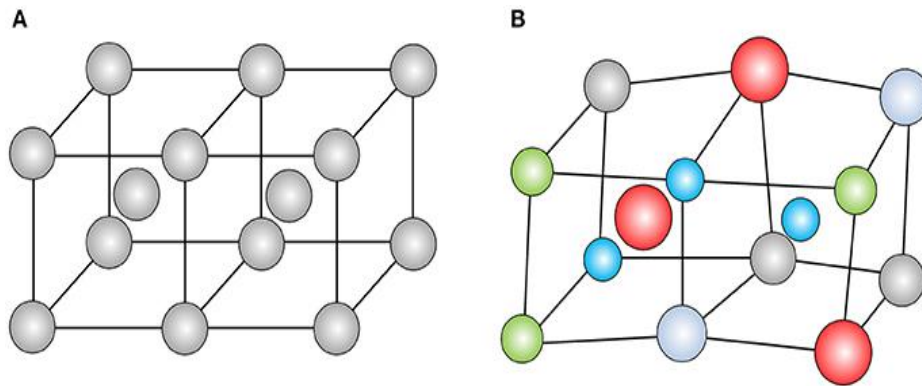


Figure 1.2 lattice distortion in HEAs^[52]

1.2.1.2 Sluggish diffusion effect

Sluggish diffusion effect of HEA can be simplified through analysis of binary system instead of quinary system. In comparison with pure metal and stainless steel, diffusion rate in HEA is way slower. Diffusion in materials are strongly dependent required energy to propel migration of atoms dislocations, vacancies and so on. This effect can be manipulated through adding certain component. For example, the addition of Ni can greatly enhance this effect by generating higher activation energies for atom migration.

1.2.1.3 High entropy effect

Thermodynamic properties are closely related to Gibbs energy, enthalpy and entropy. Their relation can be expressed by following equation: $G=H-TS$. In respect of HEA, this relation can be described in other way: $\Delta G_{mix} = \Delta H_{mix} - T\Delta S_{mix}$, where G_{mix} , H_{mix} and S_{mix} indicates mixing free energy, mixing enthalpy and mixing entropy respectively. H_{mix} is strongly corresponding to atomic size

variation. All component in HEA have similar enthalpy which propel a smaller H_{mix} . The mixing entropy of S_{mix} can be established through calculation $S_{mix} = R \sum_1^{n'} x_i \ln x_i$, where R and x_i indicates gas constant and atomic ratio respectively. Therefore, due to increasing mixing entropy along with rising number of elements of equimolar alloys, HEA is more stable due to its lower ΔG_{mix} ^[27].

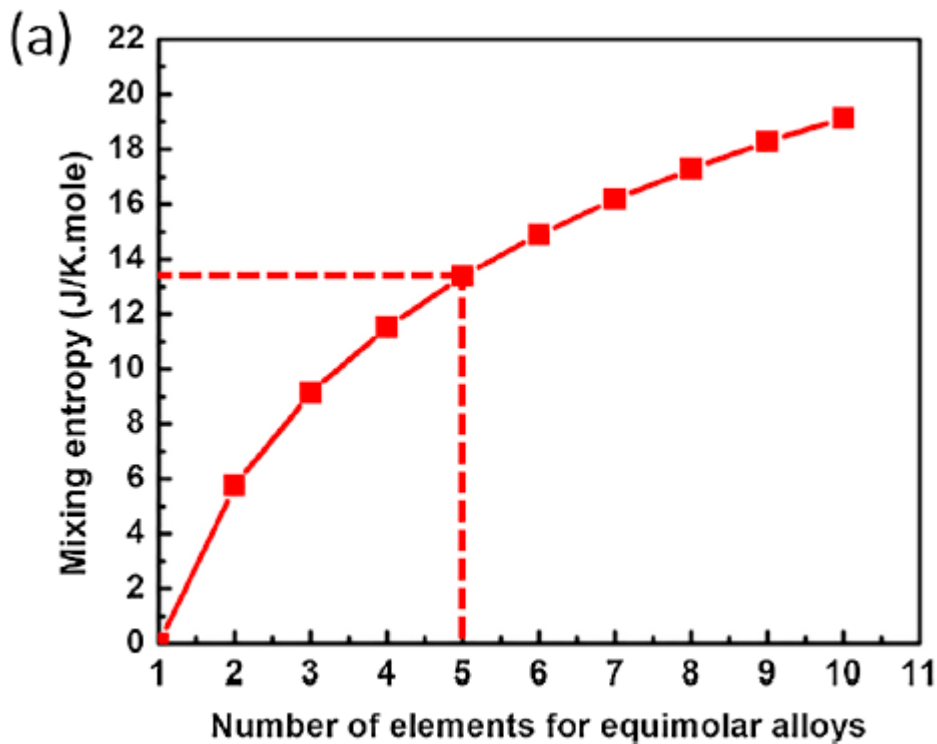


Figure 1.3 (a) Influence of number of equimolar elements on the mixing entropy of the system^[27]

1.2.1.4 Cocktail effect

Cocktail effect indicates that in HEA with multiple metallic components, the mechanical properties of HEA can easily adjusted by changing composition of one single element. This effect was first discovered by Ranganathan^[28]. This effect can also be represented by changing the composition of boron in NCATB HEA. For instance, in NCATB HEA, an addition of slim amount (0.05 at%) of boron will

propel the formation of Ta₂B compound which greatly suppresses $\beta - NiAl$ grain boundary precipitates and enhances the ductility.

1.3 Deformation induced Martensitic transformation

The martensite transformation is defined as a diffusionless process. Comparing to diffusionless phase transformation, diffusional transformation acquires no manipulations of movement of each atom, which leads to uncertain commences of atoms in lattice. However, in terms of diffusionless transformation, the distance between atoms will change correspond to the proceeding of the phase transformation, however, the relative position between atoms will not change. The martensitic transformation is commonly divided in to two categories based on thermodynamic, athermal induction and mechanical induction. As the matrix phase in martensite transformation is FCC- γ phase transforms into BCC- α /BCT- α' phase. This process will be promoted if the sufficient cooling speed is applied, there is no enough time for the diffusion of carbon atoms, which will cause the severe lattice distortion^[1]. When temperature goes under M_s (martensite start temperature), the martensite starts to form and it will complete under M_f (martensite finish temperature). The martensite start temperature is strongly dependent on aging time and temperature. The M_s temperature under various aging time and temperature is shown in Fig.3.10 Recently, considerable researches have been done to understand the martensite transformation under stress load without changing temperature. Superelasticity also known as pseudoelasticity is a reversible transformation

between austenite and martensite when external stress is applied without temperature dependence. The repeated cycle of $\gamma - \alpha - \gamma$ (fcc-bcc-fcc) of Fe-Ni alloy shows the grain refinement and the increasing density of dislocation^[2].

The feature of superelasticity was widely applied to shape memory especially in Fe-Ni-Co system for seismic protection structures. In terms of athermal induced martensitic transformation, the required driving force is compensated through rapid cooling like quenching. Yet, the deformation induced martensitic transformation (DIMIT) would appear when sufficient loading is applied. The necessary driving force for phase transition is supported by external loading. It can be mainly divided into two department “stress induced” and “strain induced depending on the required force to propel phase transformation. When necessary force to form martensitic transformation $\sigma_{\gamma \rightarrow \alpha'}$ is smaller than yield stress, it's known as stress induced martensitic transformation, otherwise, it's strain induced martensitic transformation^[57]. Increasing number of dislocation and density is also corresponding to the applied stress, which contribute to a higher internal energy^[3].

The effect of applied stress on martensitic transformation can be explained by Patel's research^[66]. They proposed that through applying compression or tension loading, the M_s of temperature would change due to compensation of driving force done by plastic work. Through derivation of Mohr's circle, we have the relation $\tau = \frac{1}{2}\sigma_1 \sin 2\theta$ and $\sigma = \pm \frac{1}{2}\sigma_1(1 + \cos 2\theta)$, where σ_1 is applied stress on material, θ is applied stress and the targeted habit plane. The positive and negative value represents the effect of tension and compression loading. The uniaxial tension

provides normal stress along positive direction, while uniaxial compression provides normal stress pointing to negative direction. Subsequently, we have the following relation: $W = \sigma\varepsilon + \tau\gamma$. It describes that the applied stress can increase the M_s temperature. In order to lower the stored energy and dislocation density in system, it generates phase transformation^[4]. Stacking fault energy (SFE) is a paramount factor to be considered. This includes the formation of partial dislocation, twinning boundary and slip of dislocation^[5]. Distinct SFE will contribute to corresponding deformation mechanism. While for low stacking fault energy system, the increasing internal stored energy due to external applied stress tends to be compensated by the formation of twinning, the high stacking fault energy system can achieve that through other approaches such as phase transformation. The plastic deformation can be propagated through dislocation slip or formation of partial dislocation. The stable twinning fault energy γ_{stf} is found to be approximately half of stable stacking faulting γ_{ssf} in FCC metal^[7].

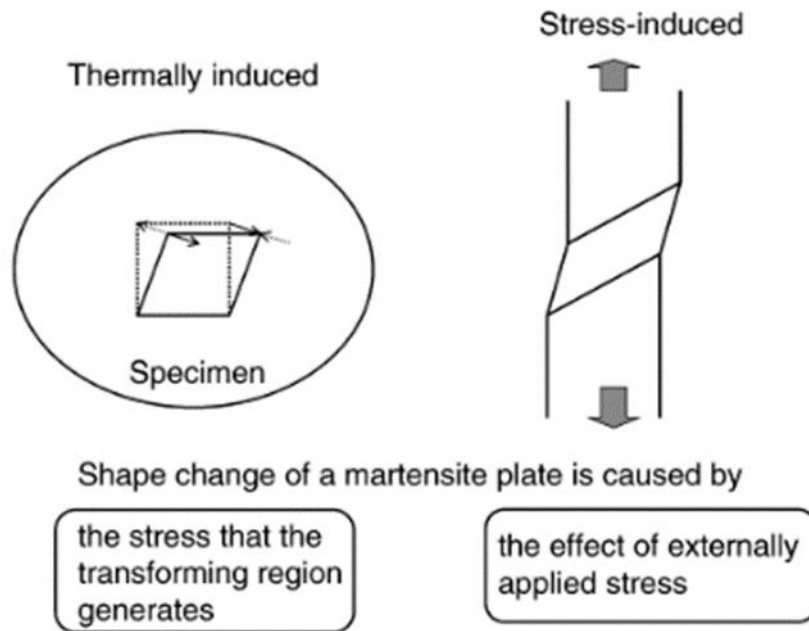


Figure 1.4 Schematic illustration of stress induced martensitic transformation ^[54].

1.4 Addition of element

The addition of certain element can be used to manipulate the morphology of martensite. In NCATB, Ni, Al, Co, B, and Ta with different atomic ratio, are significant to the manipulation of mechanical properties.

With the addition of Co in Fe-Ni system, it can enhance the hardness and foster the formation of the thin-plate martensite. Ni is widely considered as a strong stabilizer of γ matrix phase. The correlation between γ stability and M_s is studied. M_s would decrease as the increasing amount of Ni which represent a lesser favor of martensitic transformation^[32]. The influence of tantalum and boron are closely related to grain precipitation which is detailly explained in following section 2.5. Al is a significant source of $Ni_3Al-\gamma'$ nano particle and $NiAl-\beta$ (B2) grain boundary precipitate. The nano particle γ' ($L1_2$) which shares similar lattice constant with γ which associates with solid solution strengthening^[30]. Without doping B, Ta

precipitates tends to commence along with NiAl- β at grain boundaries because of similar structure they share ($a=0.3306\text{nm}$ and $a=0.2880\text{nm}$ respectively)^[31]. Moreover, Ta provide strong support to formation of γ' . The effect of doping B in NCATB HEA is further explained in part 1.5.

1.5 Precipitates in NCATB

There are several possible precipitates at grain boundaries of NCATB HEA including B-Al, B-Fe, B-Co, B-Ni, B-Ta, β -NiAl, Ta, which are strongly related to aging time and mixing enthalpy. Precipitation of Ta can provide nucleation sites for β -NiAl. However, with addition of boron, due to significantly lower mixing enthalpy of B-Ta, Ta₂B is more energetically favorable than other components. Besides, Ta₂B turns out to have distinguished tetragonal lattice structure with lattice constant equals to 0.5779nm. Due to severe lattice mismatch between Ta₂B and β -NiAl, the formation of Ta₂B suppress the precipitation of β -NiAl. Unlike strengthening effect carried out by γ' -Ni₃Al, β -NiAl contributes unfavorable brittleness of materials, therefore, limiting formation of β -NiAl is paramount to optimize ductility in NCATB HEA. On the other hand, γ' -Ni₃Al plays as an interstitial solid solution phase in the matrix of γ austenite. With an appropriate aging treatment (time and temperature), γ' -Ni₃Al is able to stabilize the solvent phase and raise energy barrier for dislocations to move. However, this mechanism might be compromised under certain situation. More specifically, ordered and

disordered solid solution phase will contribute to different mechanical properties in NCATB HEA.

1.6 Strain rate effect

Varied strain rate is significant in terms of strain hardening and deformation induced martensitic transformation. Varied strain rates are achieved through quasi-static and Hopkinson bar compression test. It was firstly proposed by Neff^[33] that high strain rate would weaken the trend for martensitic transformation due to adiabatic deformation carried by it. However, this conclusion is overthrown by Hecker^[34] and Murr^[35]. They reported that ability of martensitic transformation not only depends on strain rate but also strain level and temperature rise in shear localization area. Other than the effect caused by temperature rise along with adiabatic deformation, the strain rate effect on martensitic transformation can also be attributed to distinct yield stress. As the yield stress of materials under high strain rate deformation is higher than that value in low strain rate deformation.

1.7 Shear localization

Theory for shear localization was first developed by Zener and Hollomon^[50]. Shear localization is a phenomenon which always be presented under high strain rate. It presents under plastic deformation and within a very narrow band region. It can be triggered through many methods such as high strain rate compression, tensile test, ballistic impact and torsion test. Besides, shear localization is closely related with

formation of shear band and thermal softening. Although lots of researches support that shear bands are mainly contributed by thermal softening, however, the relation between shear bands and thermal softening remains unclarified.

1.8 Microbands

Microband is widely considered as a small angle ($\leq 8^\circ$) misorientation commences in crystalline structure materials. This phenomenon always occurs at the preliminary stage of deformation for materials acquire medium or high stacking fault energy, while it's very hard to see a microband in low stacking fault energy material^[61]. It mainly consists of double dislocation cells (dislocation walls) which are commonly comprised of screw and edge dislocation and with width around $0.4 \mu m$ and length with $10 \mu m$. However, those values are also dependent on grain size and deformation displacement. As displacement increases, the microband will be elongated and thickened until it encounters grain boundary. The formation of this band structure can be mainly attributed to shear strains and it tends to occur at smallest strain level under high strain rate. The dislocation wall can be regarded as a kind of low-angle grain boundary. Moreover, the structure mismatch between matrix and that in microband can be compensated through formation of Lomer-Cottrell locks^[62] and Lomer locks. One of the most famous theory of its formation was reported by Jackson^[63]. It is the cross-slip of dislocation which contributes to double wall feature of microbands. The cross-slip is caused by the slipping of dislocation on cross-slip plane due to local stress. However, due to the high stacking fault feature of NCATB HEA, the cross-slip dislocation will be hindered by Lomer-

lock. Under high strain rate, the density of dislocation drastically increases which leaves insufficient time for propagation of dislocation. At initial stage, slip bands would form, which subsequently contributes to the polarization of dislocations. Subsequently, due to the annihilation between dislocations, center part of the slip band will be acquired lower dislocation density but a higher internal stress. In order to relax the stress in the slip band, secondary slip system will be activated, while the wall of slip bands mainly contains primary slip system. In result, dislocation will intertwine together through interaction between primary and secondary slip system, the Lomer-locks caused by interaction between perfect dislocation commence and the misorientation cause by rotation occurs between walls. Formation of microband delivers positive effect on mechanical properties such as enhanced strain hardening ability and ductility. However, this phenomenon mostly commences in materials have relatively high stacking fault energy which suppresses martensitic transformation. Therefore, the effect of microbands on martensitic transformation remains unclear.

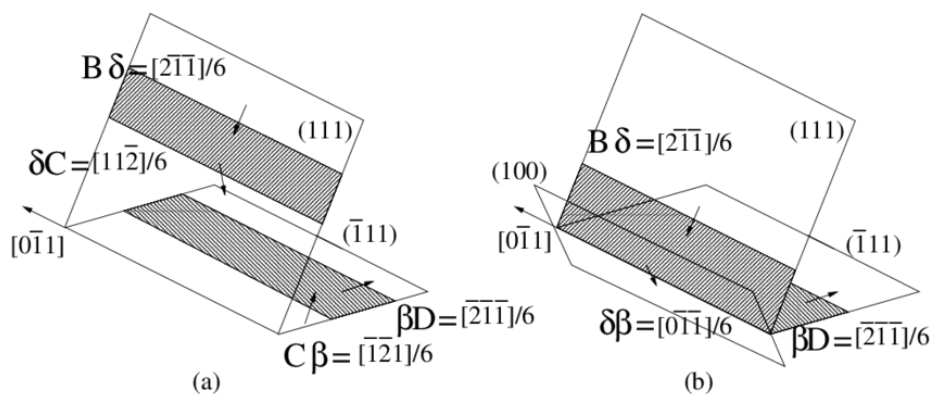


Figure 1.5 Schematic of Cottrell-Lomer lock (interaction between two partial dislocation)^[64]

1.9 Scanning transmission electron microscope

STEM functions as a combination of scanning electron microscope (SEM) and TEM. Scanning transmission electron microscope (STEM) has distinct feature with transmission electron microscope (TEM) in terms approach to obtain images. While for TEM, focused electron beams are shot through specimen plane with thickness smaller than 200nm perpendicularly, in terms of STEM, beam is focused on specimen plane with large angle. Specifically speaking, STEM has a unique detector high angle annular dark field (HAADF) detector, which provides analysis for high angle scattering electron beam.

2. Experiment and method

2.1 Fabrication method

Materials was fabricated through arc melting furnace with high purity raw materials. The purity of raw materials is present in list below:

Table 2.1 Purity of various raw materials for arc melting synthesis.

Component	Purity
Fe	99.95%
Ni	99.9%
Co	99.9%
Al	99.9%
Ta	99.9%
Ni ₂ B	99%

Due to distinct boiling melting temperature among them, they are placed in specific order in argon atmosphere to avoid loss of materials due to vaporization. An ingot was obtained after arc melting, hot rolling (1250°C) and cold rolling was performed. Aging treatment was subsequently conducted under 600 °C for 24h.

2.2 Microstructure analysis

2.2.1 XRD

X-ray diffractor (XRD) is performed to examine matrix crystalline structure and possible determination of γ' solid solution phase.

2.2.2 EBSD

The establishment of average grain size was achieved through EBSD (Electron back scatter diffraction). Other than information of grain size and grain orientation can also be reviewed. More importantly, distinct structure between matrix phase (γ). Other than the measurement of grain size and grain orientation, the GND (Geometrically necessary dislocation) density and grain orientation profile are obtained through EBSD analysis, where can be conducted to establish the rough dislocation density in NCATB HEA and crystalline misorientation caused by microbands.

2.3 Quasi-static & Dynamic compression test

In order to have better overall understanding of mechanical behavior under different strain rates. Two cylindrical specimen and one hat shape specimen with different dimensions were tested under room temperature ($T=298K$).

2.3.1 Quasi-static compression test

The Instron Model 3367 was conducted for the quasi-static compression test. The cylinder sample was well prepared by thoroughly polished its upper and lower surfaces with SiC papers. On top that, the upper and lower surface of sample were assured to be flat and paralleled. The loading stages were cleaned with methanol to avoid error. The original data with loading equals $kg \cdot N$ was converted to pascal (Pa) in order to have stress strain curve. The strain rate was set to $10^{-3}/s$.

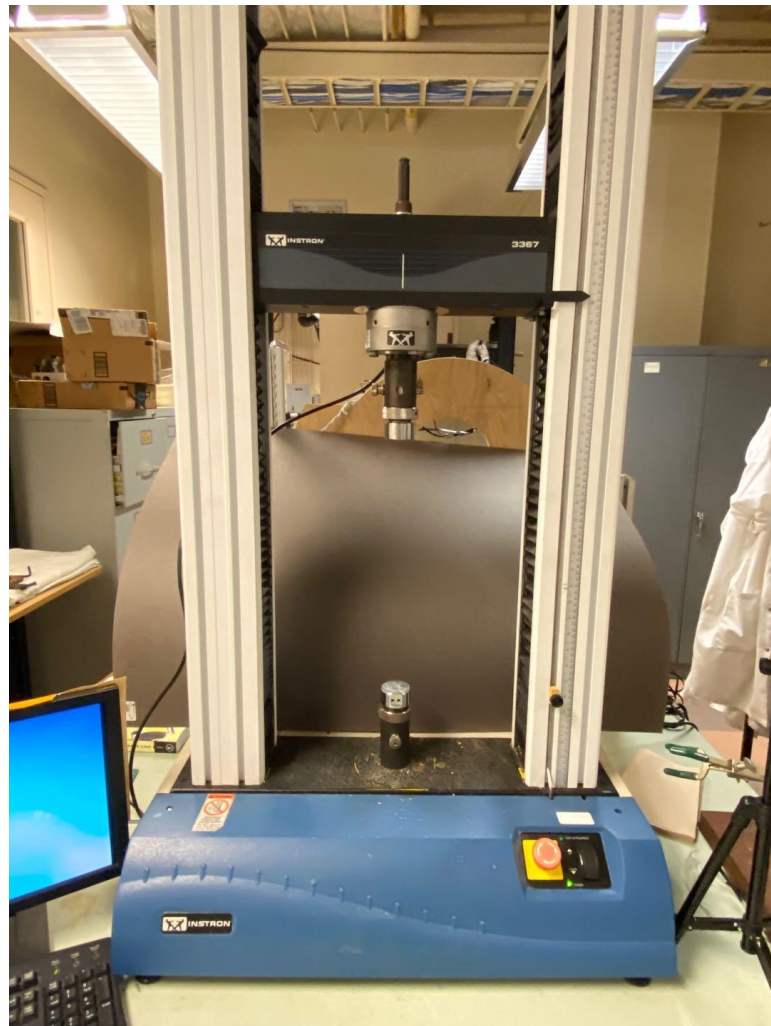


Figure 2.1 Instron quasi compressor.

Sample dimension is given in table below:

Table 2.2 Dimension of specimen for quasi-compression test.

Diameter (mm)	Height (mm)
3.6	5.4

2.3.2 Dynamic compression test

Split Hopkinson pressure bar (SHPB) is one of most widely used facility to analyze stress strain curve of materials under high strain rate which can reach as high as $10^3/s$. It was first introduced by Kolsky back in 1949^[23].



Figure 2.2 Split Hopkinson pressure bar.

Main components of SHPB mainly includes gas chamber, strike bar, incident bar, transmission bar, oscillator, lead plate, strain gauges and amplifier. Two gauges on transmission bar and incident bar respectively to obtain higher precision of data. All bars are made of maraging steel in order to have a good match with high strength alloy specimen. The applied load was modified through changing pressure in gas chamber. The wave velocity C_0 was estimated through equation $C_0 = \sqrt{\frac{E}{\rho}}$, where E

and ρ indicate young's modulus and density respectively. Through analyzation of pulse signal obtained at oscillator, wheatstone bridge was applied. Finally, we have peak signals attribute to incident wave, transmitted wave and reflected wave. Given the wave signal, we can establish the engineering stress, engineering strain and strain rate through following equation:

$$\dot{\varepsilon} = \frac{-2C_0}{L_s} \varepsilon_r(t)$$

$$\varepsilon_e = \frac{-2C_0}{L_s} \int_0^t \varepsilon_r(t) dt$$

$$\sigma_e = \frac{A_0}{A_s} E_0 \varepsilon_t$$

where

$C_0 = \text{sound speed in bar}$

$\dot{\varepsilon} = \text{strain rate}$

$\varepsilon_r = \text{reflected strain}$

$L_s = \text{length of specimen}$

$\varepsilon_e = \text{engineering strain}$

$A_0 = \text{cross sectional area of bar}$

$A_s = \text{cross sectional area of specimen}$

The diameter of the incident and transmitted bar is measured with value of 19.5mm. The calculation toward engineering stress and strain, true stress and strain, strain rates are achieved with equation below:

$$\sigma_t = \sigma_e(1 + \varepsilon_e)$$

$$\varepsilon_t = \ln(1 + \varepsilon_e)$$

The dimension of the cylindrical specimen and hat shape specimen are listed in the table below:

Table 2.3 Dimension of cylindrical specimen for dynamic compression test

Diameter (mm)	Height (mm)
3.6	3.76

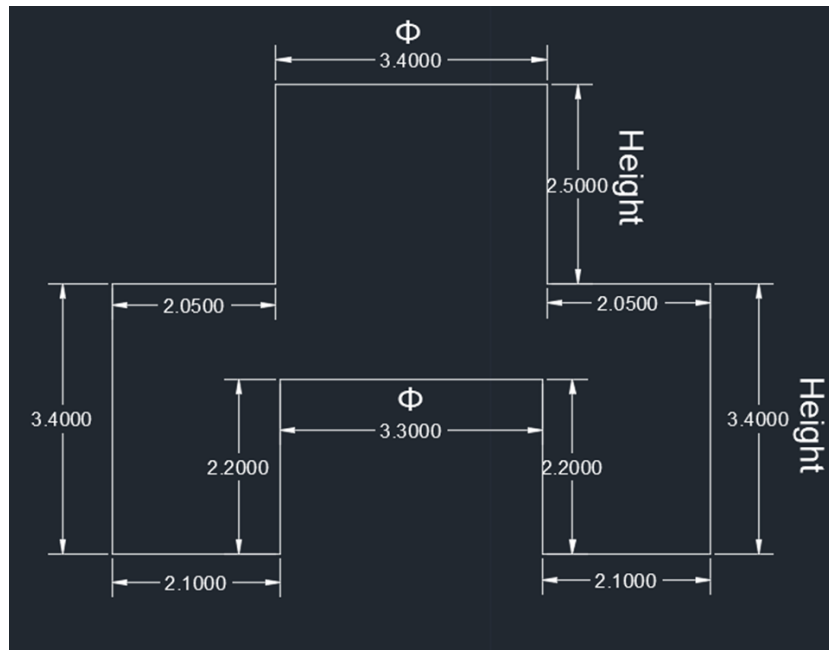


Figure 2.3 Dimension of hat shape specimen for dynamic test.

Due to more focused area of shear strain and deformation, hat shape specimen is widely used for the study of shear localization. The focused deformed is assumed to be the cross-sectional area A_s in hat shape specimen, which is shown in the following figure:

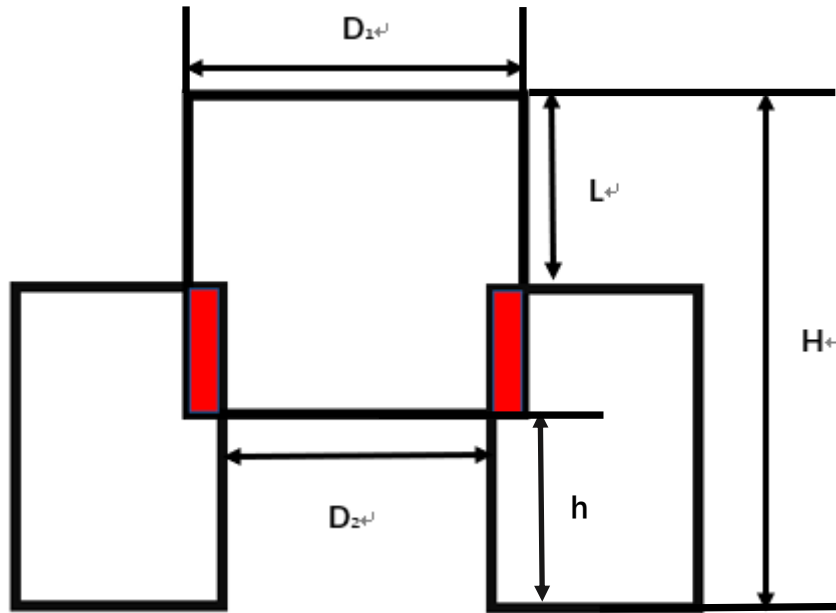


Figure 2.4 Configuration of shear strain area in hat shape specimen.

The measurement of cross-sectional area is shown in equation below:

$$A_s = \pi \times \frac{D_1 - D_2}{2} \times (H - L - h)$$

The calculation of shear strain, shear stress and shear strain rate were carried out through equation below:

$$\gamma_e = \frac{-2C_0}{w} \int_0^t \varepsilon_r(t) dt$$

$$\tau_e = \frac{A_0}{\pi A_s} E_0 \varepsilon_t$$

$$\dot{\gamma} = \frac{-2C_0}{w} \varepsilon_r(t)$$

where w is width of shear deformation area.

2.4 Chemical composition analysis using EDX

EDX test was carried out to verify possible uneven distribution of elements due to grain boundary precipitation. On top of that, EDX was also performed to confirm the uniform distribution in material.

2.5 Lamella lift out

Focus ion-beam was carried out to cut out small lamellar specimen for the further analysis in TEM. The lamellar specimen with width around $1\mu m$ was lift out from bulk sample with probe. The lamellar specimen was further attenuated into 100nm thick. Eventually, specimen was attached on TEM grid.

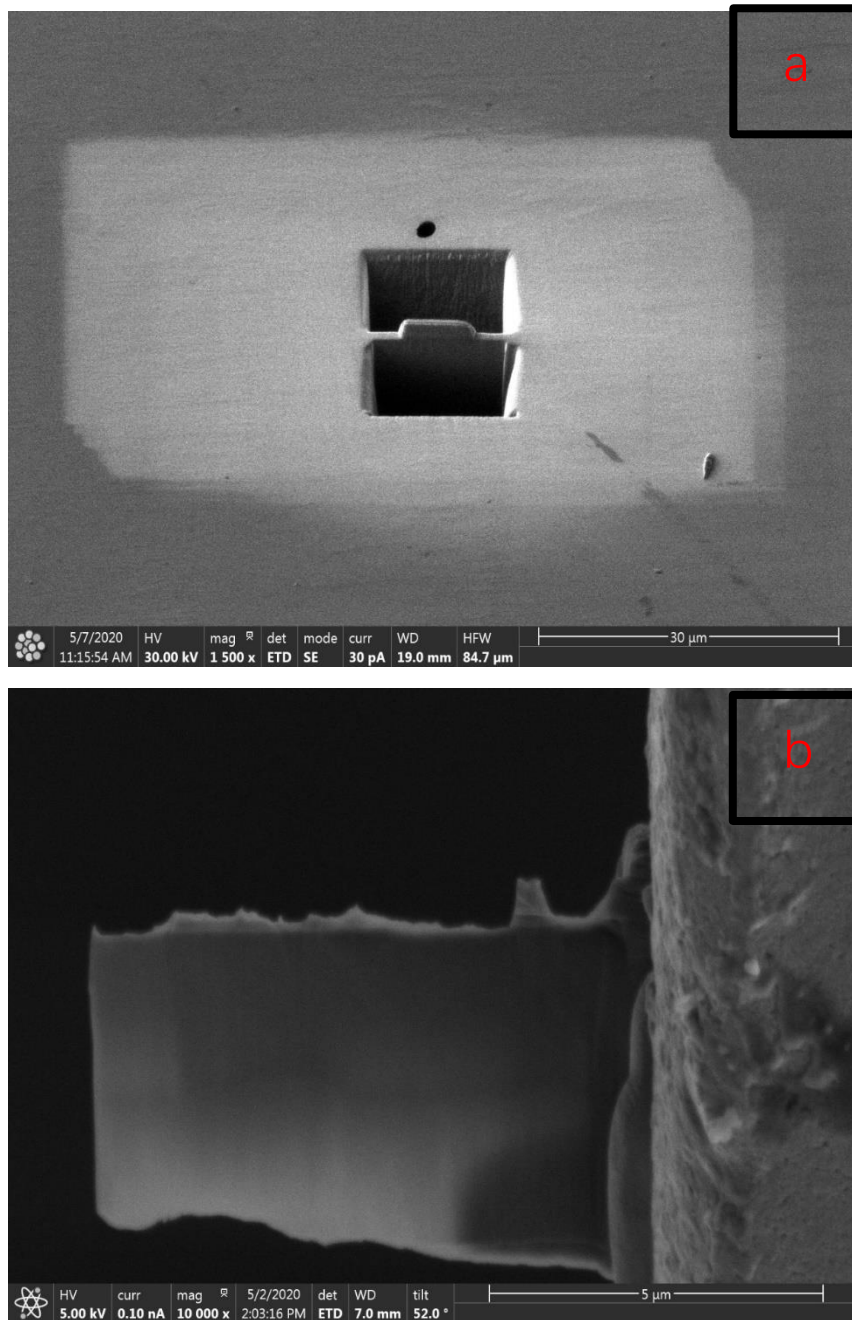


Figure 2.5 Ion beam cutting and thinning.

2.6 Etching and polishing

Etching is a necessary procedure for clear observation of grain boundaries and solid solution precipitates.

Considering there are very few researches for the reference of etching, a less strong etching solution with 12.5ml C₂H₅OH+12.5ml was used. The etching procedure lasts for 20 seconds then the specimen was rinsed with ethanol.

2.7 Scanning transmission electron microscope (STEM)

Scanning transmission electron microscope was conducted on cylindrical specimen, deformed under dynamic compression at room temperature (T=298K). Through analysis of STEM, more information of shear band formation, solid solution precipitates and martensitic transformation can be provided. High resolution images of atomic alignment can represent possible occurrence of partial dislocation in NCATB HEA.

3. mechanical behavior

The researches of mechanical behavior of high entropy alloys (HEAs) are mainly focusing on the optimization of hardness and strength of materials. There are various types of strengthening mechanisms. They can be mainly divided into 5 categories in respect of structure of materials: solution, precipitation in grain boundaries and matrix, grain size strengthening, dispersion and transformation strengthening (such as martensitic transformation strengthening). Strengthening mechanisms can vary significantly when they are down to specific HEA.

3.1 Hall-Petch strengthening

Hall-Petch strengthening also well known as grain-size strengthening. The grain-size of HEAs can mainly manipulated by varied fabrication method and

annealing time and temperature. The relation among grain size, aging time and aging temperature can be more detailly explained in equations below^{[36][37]}:

$$C = A_0 \exp \left(-\frac{Q}{RT} \right)$$

$$d^n - d_0^n = Ct$$

where,

$C = \text{growth kinetic constant}$

$Q =$

grain growth activation energy under absolute temperature T

$A_0 = \text{constant}$

$R = \text{gas constant}$

$T = \text{absolute temperature}$

$t = \text{time}$

This equation shows that as aging time and temperature increase, grain size would increase. The determination of Q is apparently related with the diffusion rate of slowest diffusing component in multi component HEAs, for instance the Ni element in Cantor alloy^[38]. Most of materials would follow the rule of Hall-Petch relationship which represent the grain size is oppositely corresponding to strength. The Hall-Petch relation is present in following equation^[11]:

$$\sigma_y = \sigma_{y0} + k_{HP} d^{-\frac{1}{2}}$$

where σ_y and k_{HP} indicates yield stress and Hall-Petch coefficient respectively, d and σ_{y0} are referring to grain size and reference yield stress. We can

see from the equation^[11] that strength is negatively correlated with grain size. the mechanism of Hall-Petch, is grain-boundaries play as an obstacle to impede the motion of dislocation. As the grain-size goes smaller, the larger the surface area per unit volume, corresponding with a higher surface energy. Given increasing surface energy per unit volume, the harder dislocations are able to overcome the energy barrier to slip through grain boundaries^[12]. Whereas, this equation is not applicable for all situations. If the grain-size gets below 1 micrometer, which is approximately equal to the size of dislocations, the inverse Hall-Petch relation will become dominant. The increasing volume fraction of triple junction and inter-crystal region, which will give a rise to grain boundary sliding and weaken the yield strength^[14].

In our current research, as shown in Fig.3.1, the average grain size apparently surpasses 200 μm by the line intercept method, which is undesired according to Hall-Petch equation. While the coarsening grains would lower the volume fraction of grain boundaries and weaken material strength, it also provides more spaces for the propagation and growth of microband.

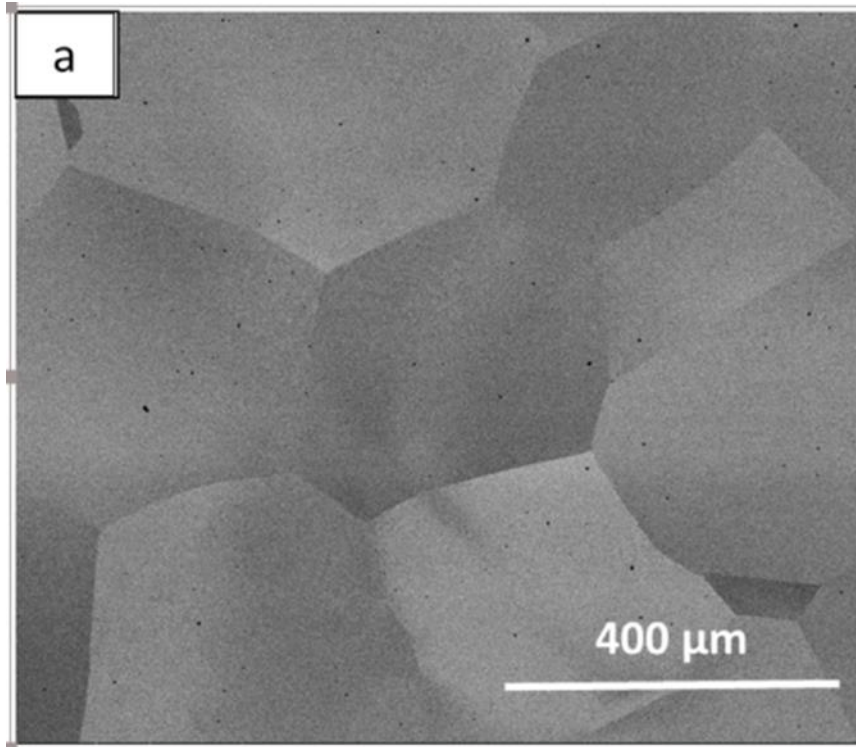


Figure 3.1 (a)SEM image of undeformed NCATB.

3.2 Strain hardening and shear localization

Strain hardening will be initialized after presence of yielding point. The strain hardening rate can be represented through the term $d\sigma/d\varepsilon$. When stress-strain curve passes its yielding point, it enters the regime of plastic deformation. The part of plastic deformation in stress-strain curve can be divided into 2 categories: strain hardening and necking. Strain hardening rate is a factor that strongly depending on the strength of materials and strain rate effect. Under high strain rate as $10^3/s$, strain hardening rate is mainly determined by adiabatic deformation instead of martensitic transformation. In contrast, low strain rate compression test present isothermal deformation. The strain stress curves for quasi-static and dynamic compression test are shown in Fig.3.2.

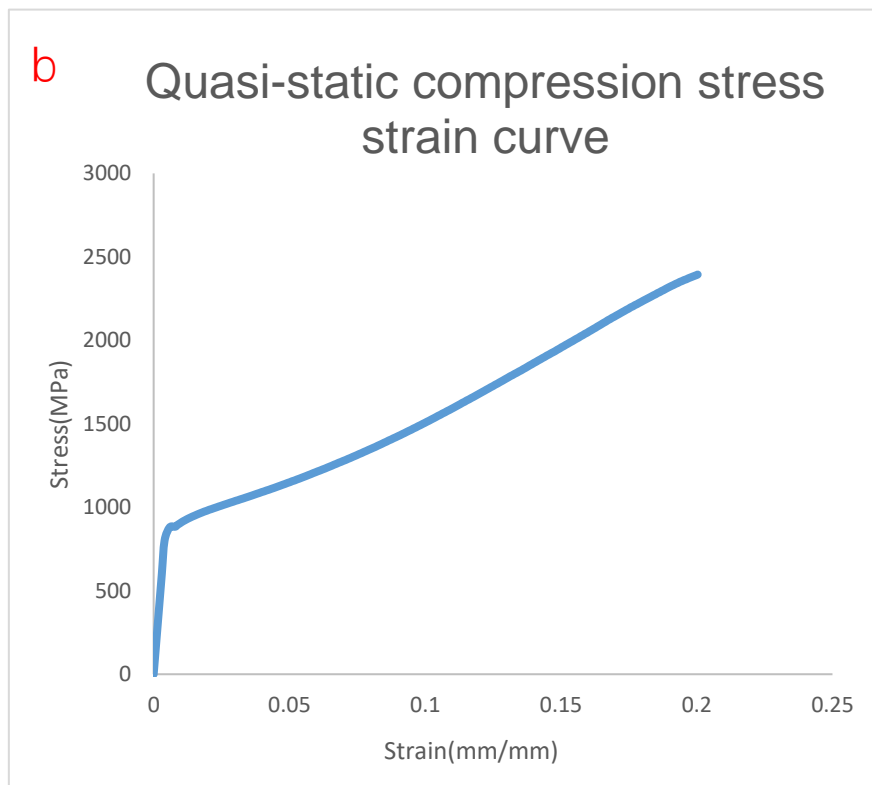
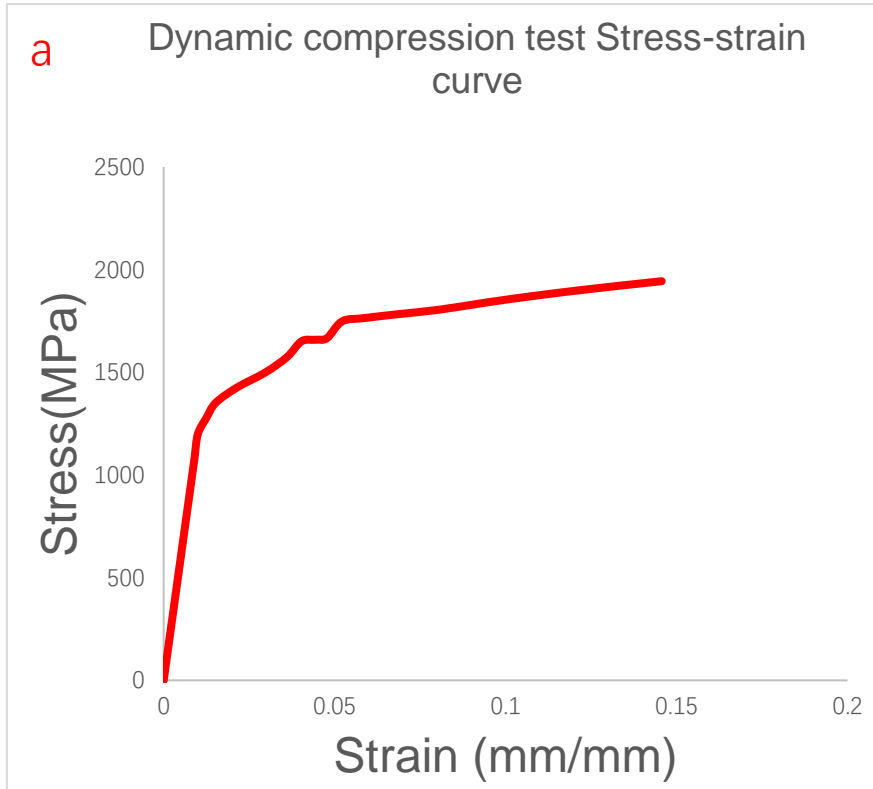


Figure 3.2 Stress strain curves for (a) Dynamic compression test (b) Quasi-static compression test

Table 3.1 Mechanical data for quasi-static compression.

Quasi-static compression	Yield stress	Strain to failure	Ultimate compression strength
	850MPa	0.20	2394Mpa

The distinct feature of these two deformation mechanisms are mainly determined by if there is sufficient time for heat dissipation at deformed region. In other word, due to short amount of time at high strain rate compression, subsequently causes significant temperature rises at deformed region. The temperature rise is explained by that the energy to propagate deformation was converted into heat^[39]. The adiabatic shear banding (ABS) is typical dynamic failure mechanism of adiabatic deformation. However, this phenomenon is widely believed to be triggered by thermal softening which is an unstable procedure when sufficient heat generates. This instability can be best represented by the jagged strain stress curve at plastic deformation regime (shown in Fig.3.2).

Besides, the instability can be compensated by high strength of materials. Adiabatic shear banding and thermal softening often appear simultaneously. However, the initiation mechanisms of shear band and thermal softening remain unclear. It is worth noted that the softening effect can be expressed by following equation^[34]:

$$\frac{d\tau}{d\gamma} = \left(\frac{\partial\tau}{\partial\gamma}\right)_{\dot{\gamma},T} + \left(\frac{\partial\tau}{\partial\dot{\gamma}}\right)_{\gamma,T} \left(\frac{d\dot{\gamma}}{d\gamma}\right) + \left(\frac{\partial\tau}{\partial T}\right)_{\dot{\gamma},\gamma} \frac{dT}{d\gamma} \leq 0$$

where $\left(\frac{\partial\tau}{\partial\gamma}\right)_{\dot{\gamma},T}$ indicates strain hardening, $\left(\frac{\partial\tau}{\partial\dot{\gamma}}\right)_{\gamma,T} \left(\frac{d\dot{\gamma}}{d\gamma}\right)$ and $\left(\frac{\partial\tau}{\partial T}\right)_{\dot{\gamma},\gamma} \frac{dT}{d\gamma}$ indicate strain rate hardening and thermal softening respectively. In the equation, thermal softening ability is negatively corresponding to strain hardening ability. It was proposed by Stout[34] that for strain level above 0.1 ($\varepsilon > 0.1$), Voce equation $\sigma = \sigma_0 - (\sigma_s - \sigma_0)\exp\left(\frac{\theta_0\varepsilon}{\sigma_s - \sigma_0}\right)$ is best suited for expression of work hardening effect. Where σ is flow stress, $\sigma, \sigma_s, \sigma_0$ are constants share same units with stress, ε is strain, θ_0 is initial work hardening rate. The temperature rise carried out by thermal softening can be measured using Taylor-Quinney relation^[41] $\rho C_p dT = \beta \tau d\gamma$, where ρ is density which is around 7.9kg/m^3 , C_p is heat capacity of material, β is Taylor-Quinney coefficient which is depending on strain rate, which It is reported by Zubelewicz that this value could be as low as 0.2-0.3 under strain rate at 1600/s and strain at 0.1-0.14 for Al2024^[42]. However, considering most of heat were generated by plastic work done by shear strain in shear band, Taylor coefficient with 0.9 is more appropriate. This equation can be further derived into form of: $dT = \frac{\beta\tau d\gamma}{\rho C_p}$. According to this, we can notice that the decreasing heat capacity or density can cause increase of instability. The shear stress and shear strain can be calculated through following equation:

$$\tau = \frac{\sigma}{2}$$

$$\gamma = \sqrt{2 \exp(2\varepsilon) - 1} - 1$$

The shear strain stress curve is derived and shown in figure below:

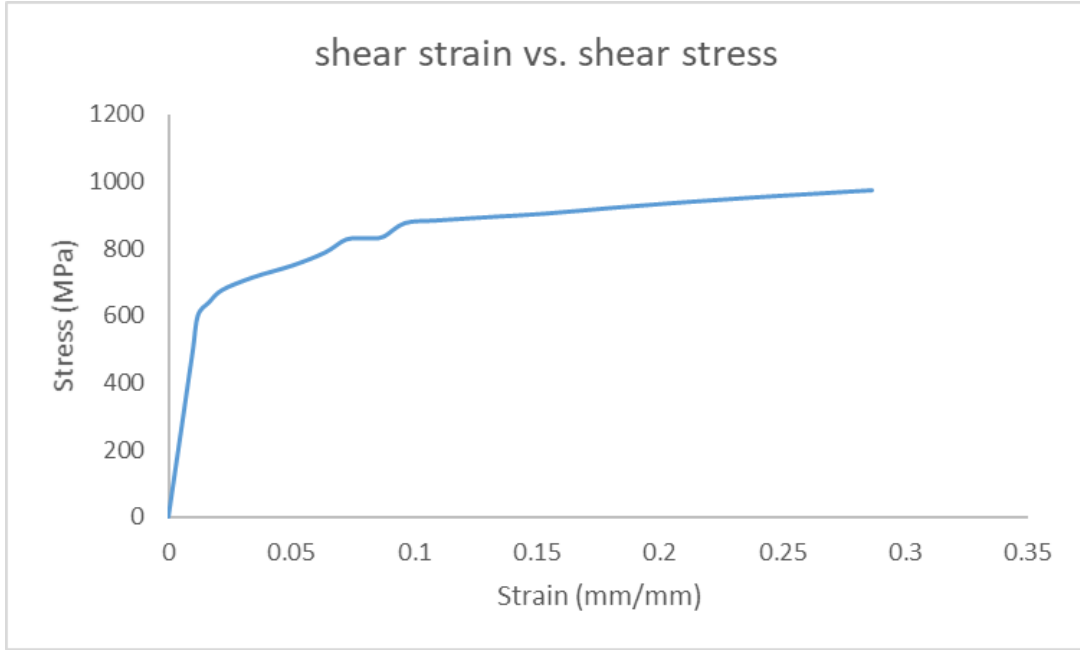


Figure 3.3 Stress strain curve.

The heat capacity of NCTAB HEA is measured through weight averaging approach $C_p = w_i \sum_{i=1}^6 C_{pi}$ (where w_i and C_{pi} indicates weight percentage and heat capacity of each element respectively), which is approximately 442.29 J/(kg K). Recrystallization could happen in shear band depending the extent of temperature. If ΔT surpass $0.4T_m$, recrystallization could present. The recrystallization happens in shear bands would lead to growth of ultra-fined grains. In order to obtain precise ΔT value, we need to find out critical strain to initialize shear band. The critical shear strain for formation of shear band which is also called ‘‘Culver criterion’’^[44]. When strain level surpasses the critical strain, effect of shear localization would be more prominent. The value of it can be expressed by following equation:

$$\gamma_c = \frac{\rho C_p n}{-\frac{\partial \tau}{\partial T} \cdot 0.9} \quad (\beta = 0.9)$$

where n is strain hardening coefficient. and $\frac{\partial \tau}{\partial T}$ represents ability of thermal softening also known as thermal softening coefficient. The thermal softening coefficient is hard to measure which requires considerable amount of isothermal experiments, and it is even more complicated for situation under high strain rate^[45]. Therefore, into order to establish appropriate critical shear strain, further researches need to be done to obtain accurate thermal softening coefficient for NCATB HEA. The strain hardening coefficient can be measured through Ludwik-Hollomon constitutive equation:

$$\tau = \tau_0 + K\gamma^n$$

$$n = \frac{d \log(\tau - \tau_0)}{d \log \gamma}$$

With data we have in shear stress strain curve in Fig.3.3 and $\log(\tau - \tau_0)$ vs. $\log \gamma$ curve in Fig.3.4, we have the n represent by the slope which is around 0.79.

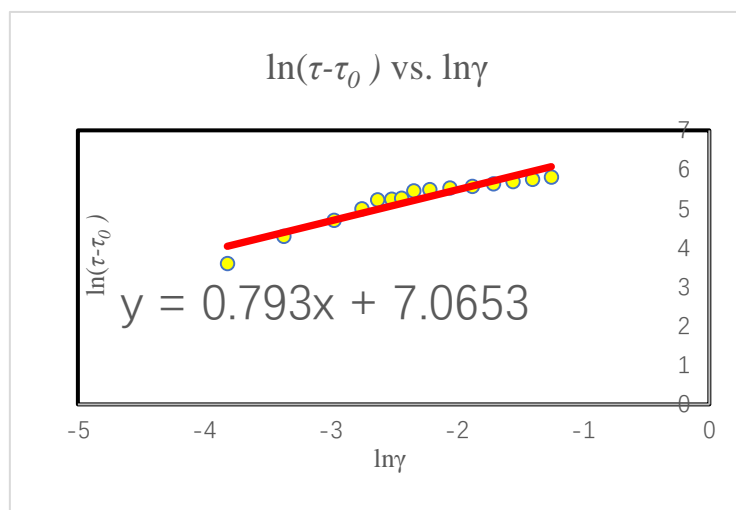


Figure 3.4 $\log(\tau - \tau_0)$ vs. $\log \gamma$ and its fitting line.

For high strength materials, they tend to have lower critical shear strain which associates with their high stability under plastic deformation.

Shear band can be divided into two categories, transformation band and deformation band where phase transformation and intense shear present at. It was proposed by Bradley that, the hardness inside shear band is higher than that in both sides of it. Moreover, the hardness will recover as it gets distant from shear band^[39].

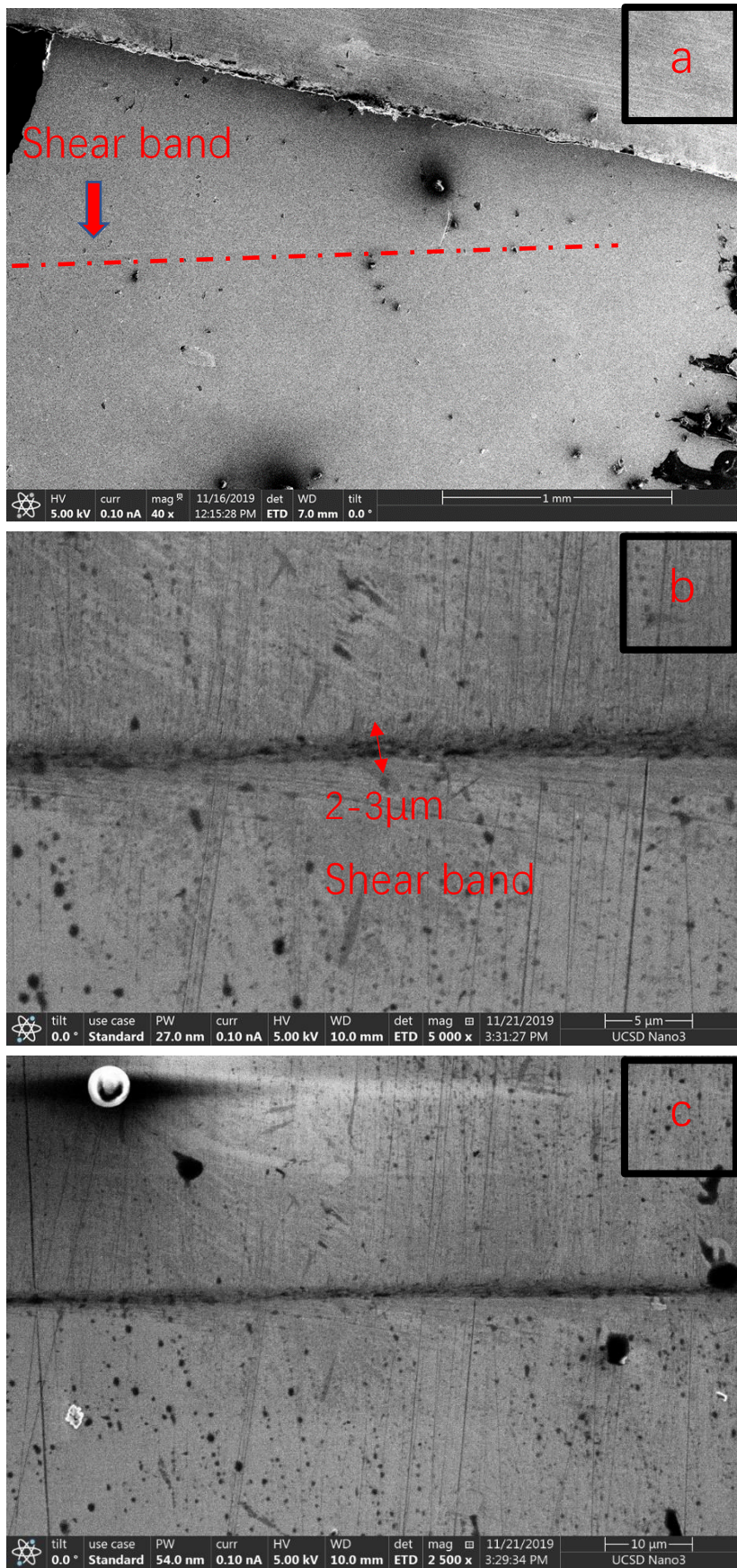


Figure 3.5 SEM image (a,b,c) of shear band.

3.3 Solid solution strengthening

In terms of solid solution strengthening, it can be greatly influenced by the effect of short-range order, concentration and so on. In order to dictate the critical resolved stress for the generation of slip, the ‘modified’ Peierls-Nabarro equation $\tau = \frac{1}{b} \max \left\{ \frac{dE_{misfit}}{du} \right\}$ is applied. Where u is displacement, E_{misfit} is referring to energy barrier function of dislocation displacement, τ is critical resolved shear stress for the movement of dislocation^[8]. E_{misfit} is related to $a_0, \gamma_{us}, \gamma_{isf}$, which represents lattice constant, required fault energy per unit area to form a slip, intrinsic stacking fault energy. According to the equation, the critical resolved stress is subject to the solute ordering. The activation volume V , when it's under plastic deformation, can be established through following equation:

$$V = bA = - \frac{\partial \Delta G(\tau)}{\partial \tau} \Big|_T = MkT \frac{\partial \ln \dot{\epsilon}}{\partial \sigma} \Big|_T$$

Where b is burger's vector, A is activation area, M is Taylor factor convert shear to normal stress ($\tau \rightarrow \sigma$), $\dot{\epsilon}$ is strain rate, $\Delta G(\tau)$ is the free energy barrier dislocations have to overcome to move. Considering FCC and BCC metals, they possess distinct activation volume, while FCC has a much higher value of V in contrast to BCC metals. For FCC metals, the forest dislocations need to be established for the determination of activation volume V . Forest dislocations spacing l can be accessed through dislocation density $\sim \rho^{-\frac{1}{2}}$. Activation volume of solid-

solution hardening and forest dislocation are conducted to determine V through following relation^[9]:

$$\frac{1}{V} = \frac{1}{V_{ss}} + \frac{1}{V_f}$$

Activation volume of forest dislocations V_f can be determined by $V_f = bwl = bw\rho^{-\frac{1}{2}}$ where w is the width of obstacle.

Activation volume of solid-solution V_{ss} can be determined through solid-solution strengthening theory established by Curtin^[11].

$$V_{ss} = \frac{0.55M}{\sigma_{ss}} \Delta E_b$$

Due to the extreme small size (nanometer scale) of solid solution precipitates, it's possible to observe them under SEM. Therefore, the verification and analysis of solid solution precipitates can be mainly achieved through TEM. The coherency between matrix and solid solution phase is crucial to stability of matrix. It is closely related to the critical precipitates size.

Based on the analysis result we obtain from XRD identification, the highest peak signal with strongest signal appears at $2\theta = 43^\circ$, which indicates the presence of FCC γ -austenite matrix phase which can also be verified through EBSD and shown in Fig.3.14. It is reported by Adarsh and his colleagues^[48] that the peak signal of γ' -Ni₃Al and β -NiAl phase might occur depending on aging time. It can be shown in Fig.38 that, as aging time increases, the XRD signals of γ' and β become more prominent. The relationship between growth rate of γ' and aging time can be explained by Ostwald ripening $R^3 - R_0^3 = kt$, where R is average precipitates radius and R_0 is initial average precipitates radius. For $t \leq 24h$, a

relation between aging time and precipitates size $R^3 - 4.2^3 = 75t$ under 700°C was reported by Zhang. Given that this material^[56] The precise particle size under different aging time is reported by Geng^[52]. Apparent increase of precipitate size would occur as elongation of aging time. However, due to no compromise of phase coherency between γ' and γ under 600°C and 24h heat treatment, Ostwald ripening relation was developed. According to the research done by Geng^[52], precipitates size for 72h is approximately 4.7nm, which should be larger than that under 24h of treatment. They also found that the critical solid solution precipitates size would emerge at 24h/ 700°C with value of 13nm. This represents when precipitates size surpasses this value, the coherency will be compromised, which weakens the stability of matrix and further rises the M_s temperature and subsequently affect the morphology of martensite. As the precipitates size reaches above a critical value, more of Ni will be consumed to form γ' , less Ni will contribute to stabilization of matrix phase, which leads to a more available martensitic transformation in matrix phase with higher M_s temperature. However, as the precipitates size get larger, the coherency between γ' and γ will be compromised.

Table 3.2 Average precipitate size of γ' at aging temperature of 600°C and 700°C 错误!未找到引用源。

Aging temperature, °C	Aging time, h	Precipitate size, nm
600	72	4.7 ± 1.7
	168	5.0 ± 1.5
	240	5.7 ± 1.1
700	5	10.0 ± 1.3
	10	11.2 ± 1.6
	15	12.1 ± 1.3
	24	13.0 ± 2.2
	48	21.5 ± 2.2
	72	30.9 ± 4.3
	240	40.1 ± 8.8

From the data we obtain in research from Fig.3.7, there is no obvious peak for γ' and β can be matched with that in Fig.3.8. The similar lattice structure between γ and γ' can account for the overlapping of two phases. There is only

small amount of β phase that occur along grain boundaries which suggests a weak signal in XRD pattern (Fig.3.7).

Therefore, further examination and verification were carried out for solid solution precipitates through TEM analysis. Under high strain rate, materials with high stacking fault tends to generate large amount of dislocation and slipping of dislocation to propel plastic deformation which can be described in Fig.3.6(a). Multiple dislocations have been found which may associates with dislocation overcoming precipitation or dislocation slip on other planes. Increasing dislocation density and precipitate size are corresponding to more often interaction between dislocation and solid solution precipitates, subsequently leading to enhancement of strength. On top of that, formation of γ' solid solution precipitates can also make great impact on morphology of martensite, as the precipitates we observed is around 3~4nm which is significantly lower than critical size. Besides, through the Fast Fourier Transformation analysis shown in Fig.3.6(c), the zone axis is along [001] direction. Based on the diffraction mechanism of TEM, if γ' solid solution particle transcends its critical size, the ordered and coherent solid solution phase will no longer exists, which will give a rise to a TEM diffraction patterns of disordered grains where plane (110) will not be shown because (110) is a forbidden plane for FCC structure along [001] zone axis. Whereas, as the ordered γ' nuclei, the forbidden plane (110) will present in FFTs. Same as the FFT pattern shown in Fig.3.6.

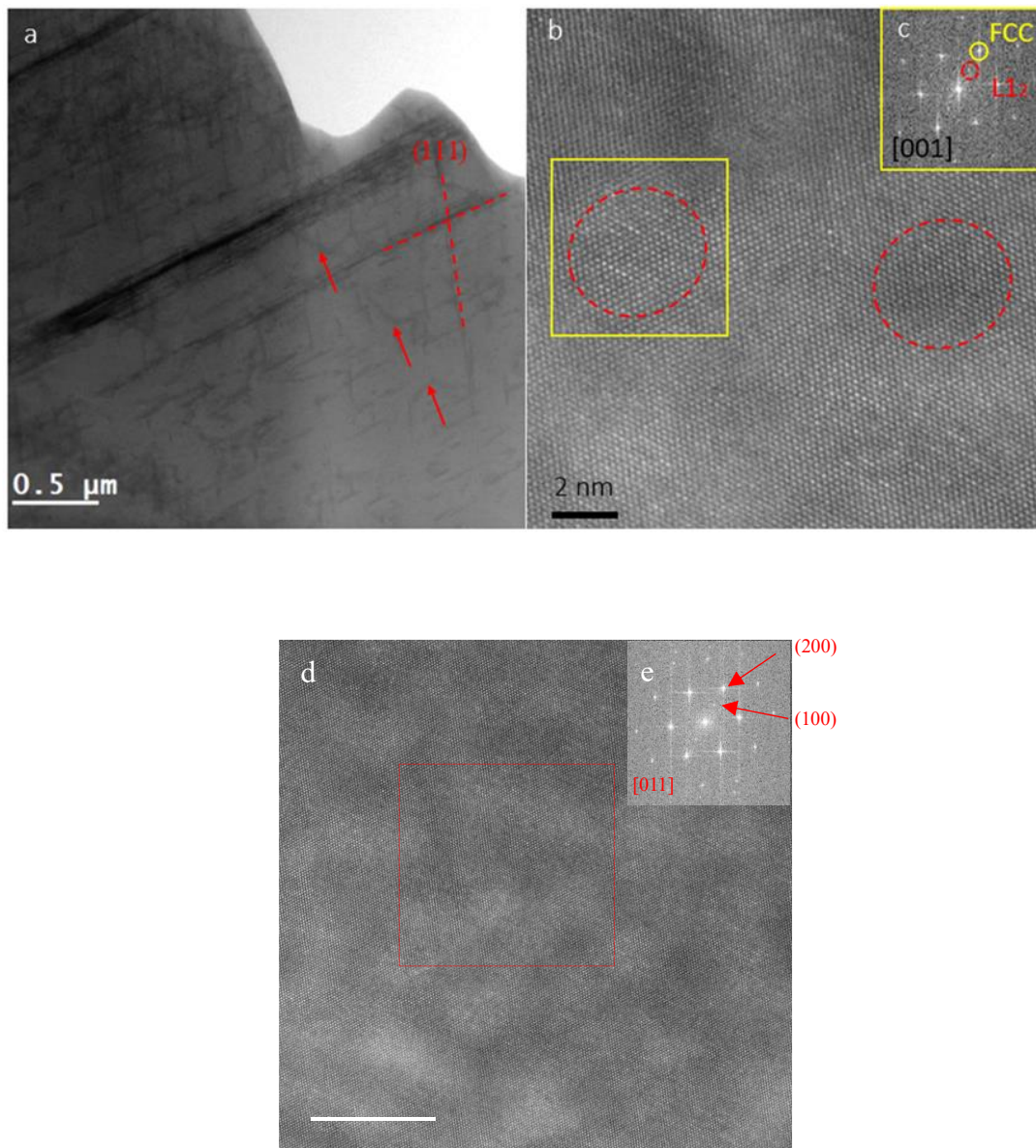


Figure 3.6 (a) STEM HAADF image shows planar dislocation slips and multiple dislocation half-loops. (b) Coherent L_{12} phases (in the red circle areas) have been observed, which were embedded in the matrix. (c) FFT (fast Fourier transformation) pattern (in the yellow box) confirms the FCC matrix structure and L_{12} precipitation structure in the $[001]$ zone axis. (d) Ordered L_{12} form in the matrix (e) FFT patten in the red box confirms the formation of L_{12} phase in $[011]$ zone axis.

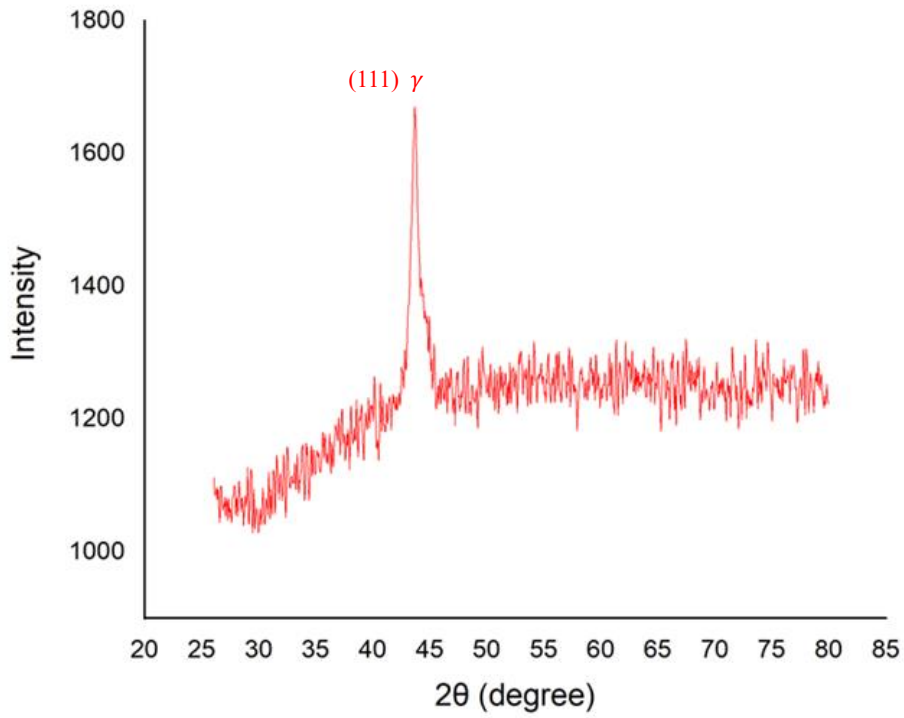


Figure 3.7 XRD result of NCATB HEA before mechanical test.

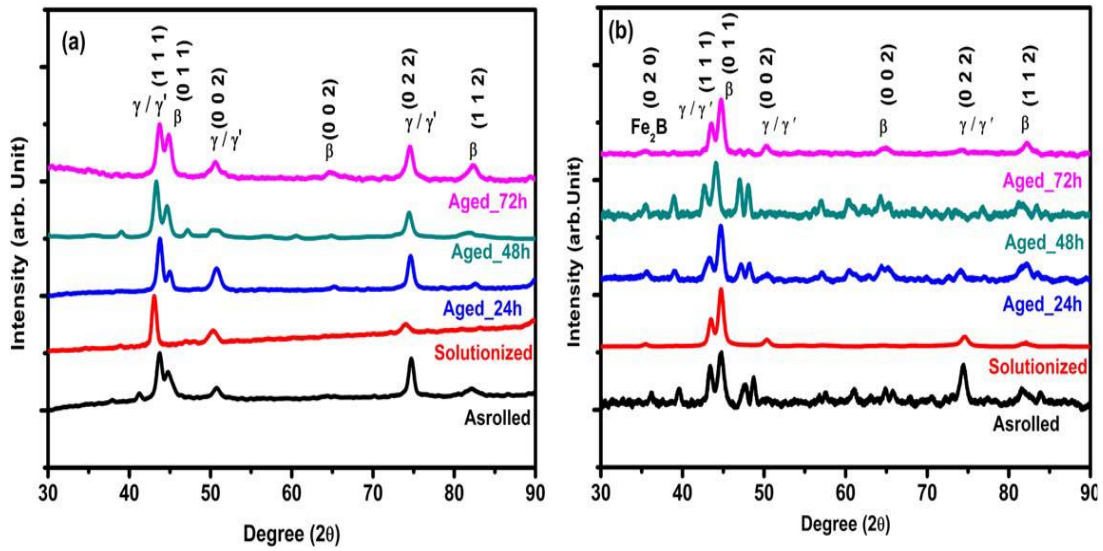


Figure 3.8 XRD patterns of NCATB HEA with different grain size ($136\mu m$ and $182\mu m$) [48].

3.4 Strain rate effect

Comparing the yield stress between quasi-static compression and dynamic compression test, we can find out a higher value of it for dynamic compression test (1100MPa and 1278MPa), which can be explained by strain effect in some extent. If we regard flow stress as a constitutive function of strain rate, temperature and strain, it can be best expressed by Johnson-Cook equation^[46]:

$$\sigma = (\sigma_0 + B\varepsilon^n) \left(1 + C \ln \left(\frac{\dot{\varepsilon}}{\dot{\varepsilon}_0} \right) \right) [1 - (T^*)^m]$$

Where σ_0, B, C, n are material constants, which correspond with yield stress under reference conditions, strain hardening constant, strain rate strengthening coefficient and strain hardening coefficient respectively. m is thermal softening coefficient. T^* can be expanded into $T^* = \frac{T-T_r}{T_m-T_r}$, where T_m is material melting temperature, T_r is reference temperature based on reference yield stress shown previously. The material constant B can be measured through neglecting thermal softening effect and set $T = T_r$, $\dot{\varepsilon} = \dot{\varepsilon}_0$. By the previous analysis we have $\sigma_0 = 1278MPa$ at dynamic compression test. Subsequently we have following modified relation^[47]: $\ln(\sigma - \sigma_0) = n \ln \varepsilon - \ln B$ and its curve is represented in Fig.3.9.

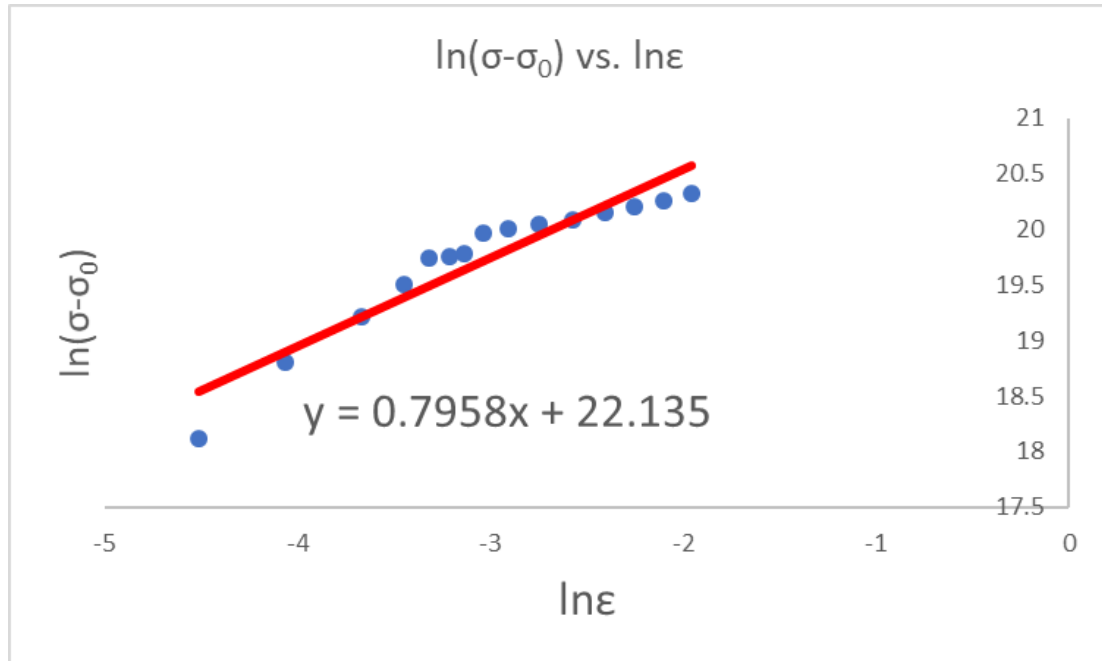


Figure 3.9 $\ln(\sigma - \sigma_0)$ vs. $\ln\epsilon$.

3.5 Martensitic transformation

Several types of deformation induced martensitic transformation could occur in iron-based alloy including: $\gamma \rightarrow \epsilon \rightarrow \alpha'$, $\gamma \rightarrow \epsilon$ and $\gamma \rightarrow \alpha'$, where $\gamma \rightarrow \alpha'$ is the most common transition in Fe-Ni and Fe-C alloy. The γ and ϵ have stacking pattern of ABCABCABC and ABABAB respectively, while α' behaves no certain stacking fault pattern due to the absence of close packed plane.

The metastable γ phase transformation to α' martensite would occur during plastic deformation region. The deformation induced martensitic transformation can be divided into stress-induced and strain-induced, depending on the critical force to form martensite. It was observed that lath-like martensite and thin plate martensite are corresponding to strain-induced and stress-induced respectively.

Moreover, the lath-like martensite is more likely to form at the highest M_s temperature, while the thin plate martensite is in the opposite. The changing of M_s temperature are mostly correlated to the variation of Ni concentration, which is corresponding to solid solution phase. Stress induced martensitic transformation is mainly abide by several index of temperature, M_s , M_d^σ , M_d^ε and M_f , which indicates martensite start temperature, stress induced martensite start temperature, strain induced martensite start martensite and martensite finish temperature respectively. The martensite start temperature is strongly dependent on aging time and temperature. The M_s temperature for 24h/600°C is shown in Fig.3.10(a), which is approximately lower than -100°C. On top of that, the critical stress for martensitic transformation $\sigma_c^{\gamma \rightarrow \alpha'}$ is also a most crucial parameter to consider. This parameter represents when localized stress reaches critical value under certain temperature, the required driving force is met, martensitic transformation occurs.

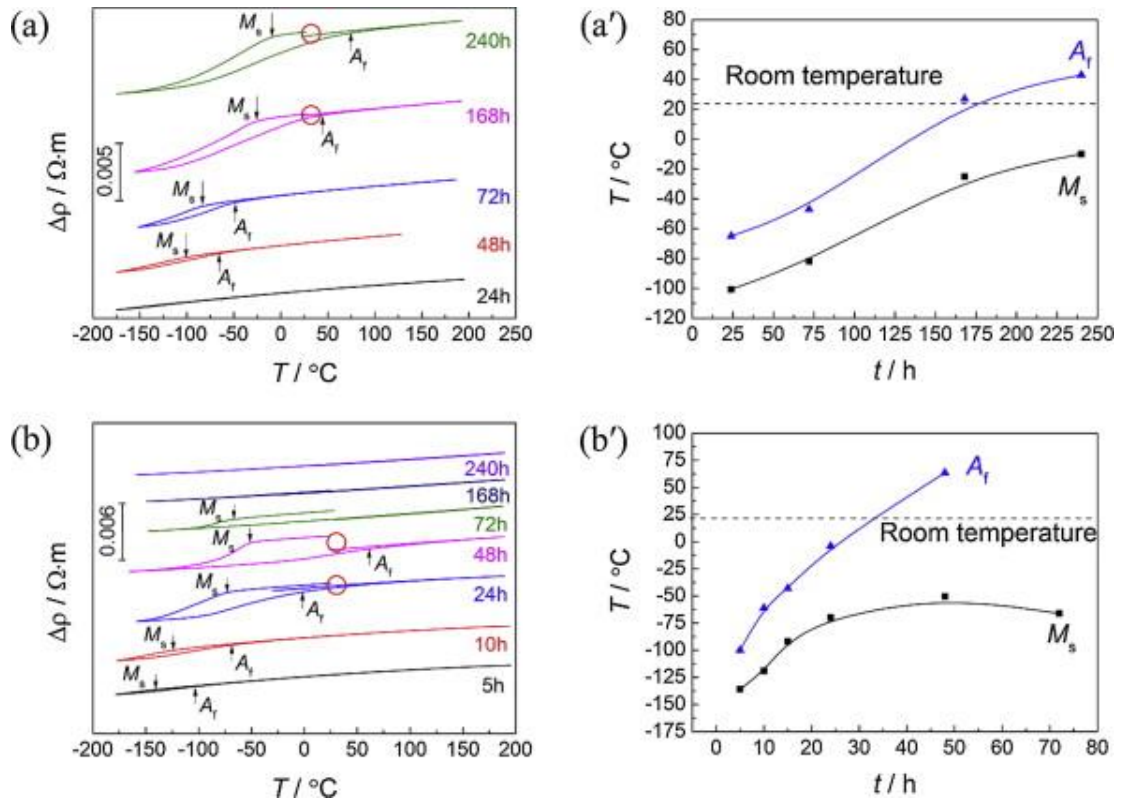


Figure 3.10 (a) Heating and cooling procedure of NCATB aged under 600°C with M_s and A_f marked (a') Various M_s and A_f of NCATB aged under 600°C depending different aging time (b) Heating and cooling procedure of NCATB aged under 700°C with M_s and A_f marked (b') Various M_s and A_f of NCATB aged under 700°C depending different aging time^[52]

The stress-induced martensite transformation occurs at temperature between M_s and M_d^σ , where M_d^σ is referring to highest temperature when stress-induced martensitic transformation can happen. As the testing temperature goes down, the volume percentage of thin-plate martensite would increase. The flow stress is determined by the amount of stress to keep the plastic deformation going. As the formation of martensite, the flow stress would increase. In respect of energy, the critical free energy barrier for the martensitic transformation is represent by $\Delta G_{crit}^{\gamma \rightarrow \alpha'}$. At temperature between M_d^σ and M_s , a complementary energy is needed through applying external loading. This energy barrier can be overcome by applying force,

and can be represent by $W_{min}^{\gamma \rightarrow \alpha'}$ ^[18]. It is shown in Fig.3.11 that, all elements are evenly distributed in materials, which exterminate the factor of uneven dispersion.

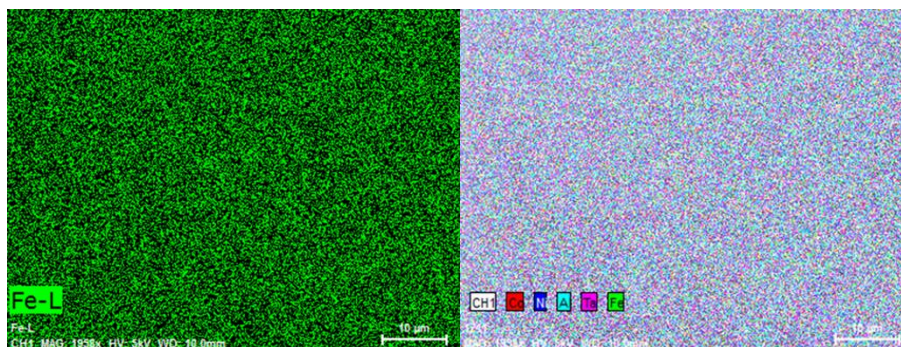
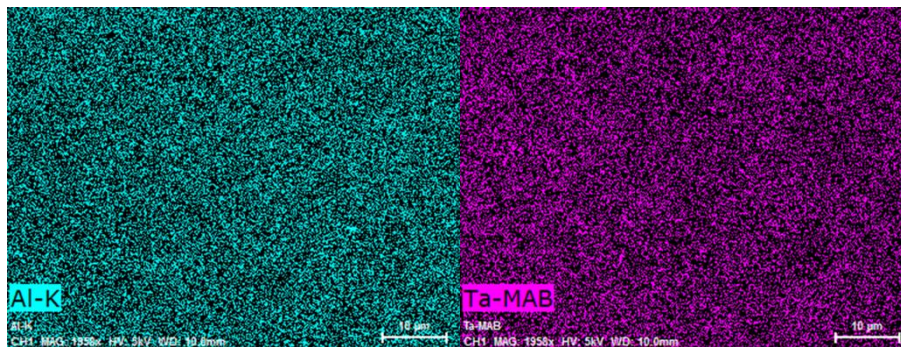
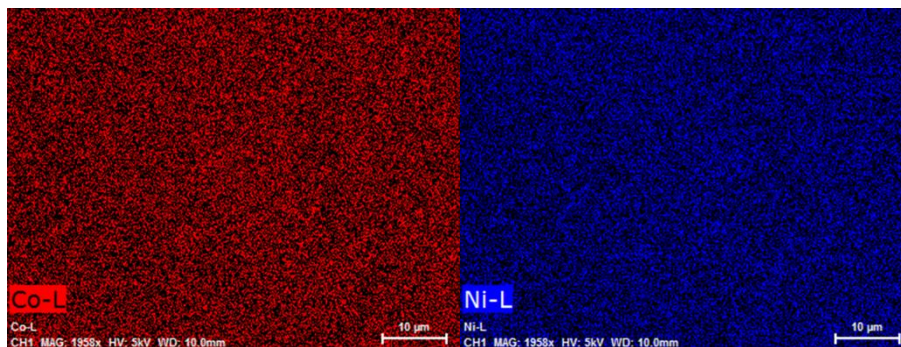
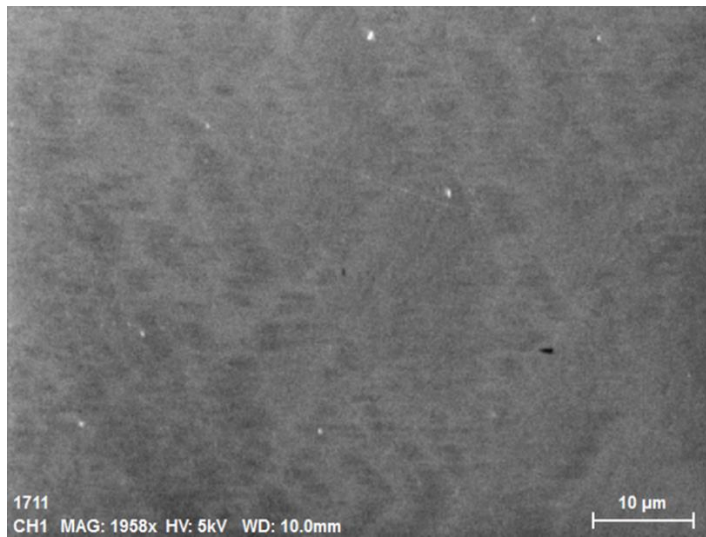


Figure 3.11 EDX configuration of undeformed NCATB materials.

3.5.1 Strain rate effect on martensitic transformation

Very few researches have been developed for NCATB alloy on high strain rate compressive test. According to previous researches, strain rate can be paramount to the commence of martensitic transformation, more specifically, $\gamma \rightarrow \alpha'$ transformation. The measurement of volume fraction of α' can be established through magnetic permeability technique. strain rate $\dot{\epsilon}$ is not the only factor to be considered, but also the strain range. At low strain level, typically, $\epsilon < 0.25$, high $\dot{\epsilon}$ will contribute to a high production of α' , however, in respect of large displacement $\epsilon > 0.25$, under low $\dot{\epsilon}$, there would be less α' . The distinct phenomenon caused by this could be owing to shear localization and changing temperature under different cases. The correlation between temperature rise and strain range for 304 stain less can be represent by following scheme Fig.3.12^[19].

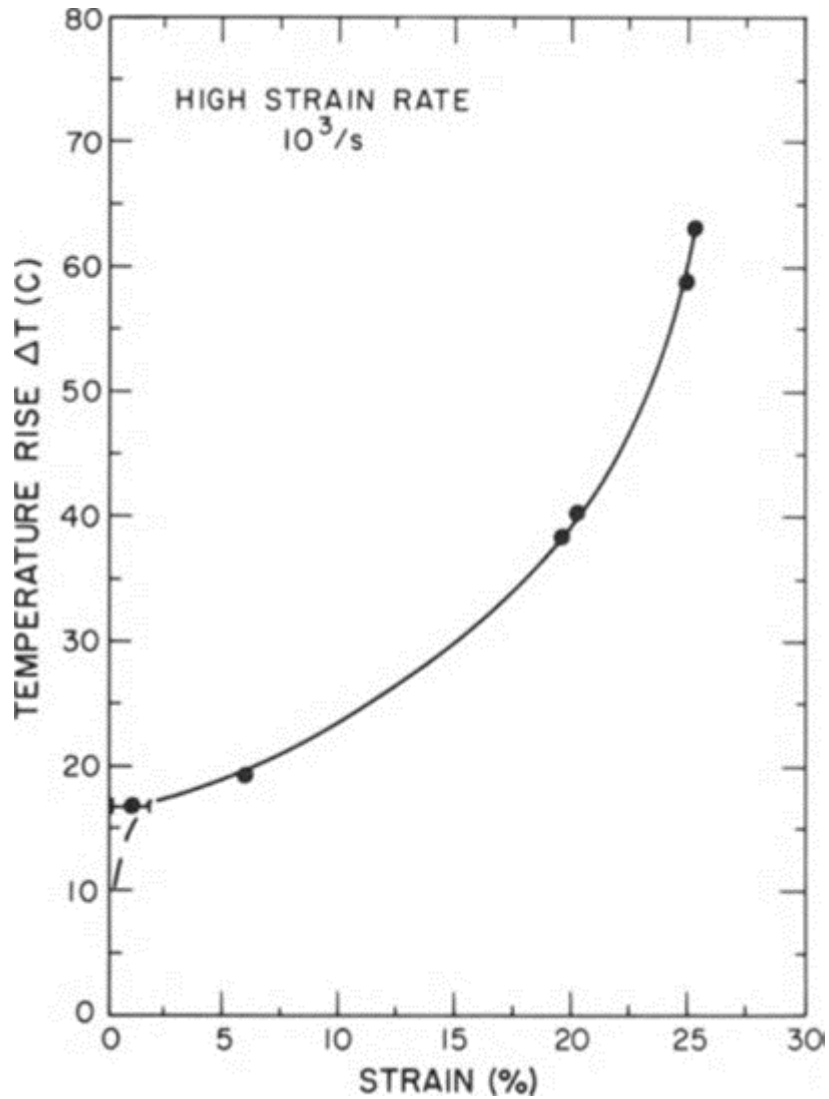


Figure 3.12 Temperature rise vs. strain^[19].

Based on the analysis of martensitic transformation developed by Olson and Cohen^[20], the nucleation sites only locate at shear band intersections, which is related to stacking faults, twins and ε . The tendency to form shearing bands is closely related to stacking fault energy, temperature, $\dot{\varepsilon}$ and α . The number of shear band intersection is described by parameter β . In order to calculate number of shear band N_V^{sb} , the following equation is present:

$$N_V^I = k(N_V^{sb})^n$$

Where k and b are constant, N_V^I is number of shear bear band intersection.

Then we can derive the volume fraction of α' as function of α and β . We can have:

$$f^{\alpha'} = 1 - \exp\{-\beta[1 - \exp(-\alpha\varepsilon)]^n\}$$

Where α indicates the rate of shear band deformation, β is probability that a martensitic embryo commences at intersection. The α/β relations with temperature are predicted by Angel^[21] (Fig.3.13).

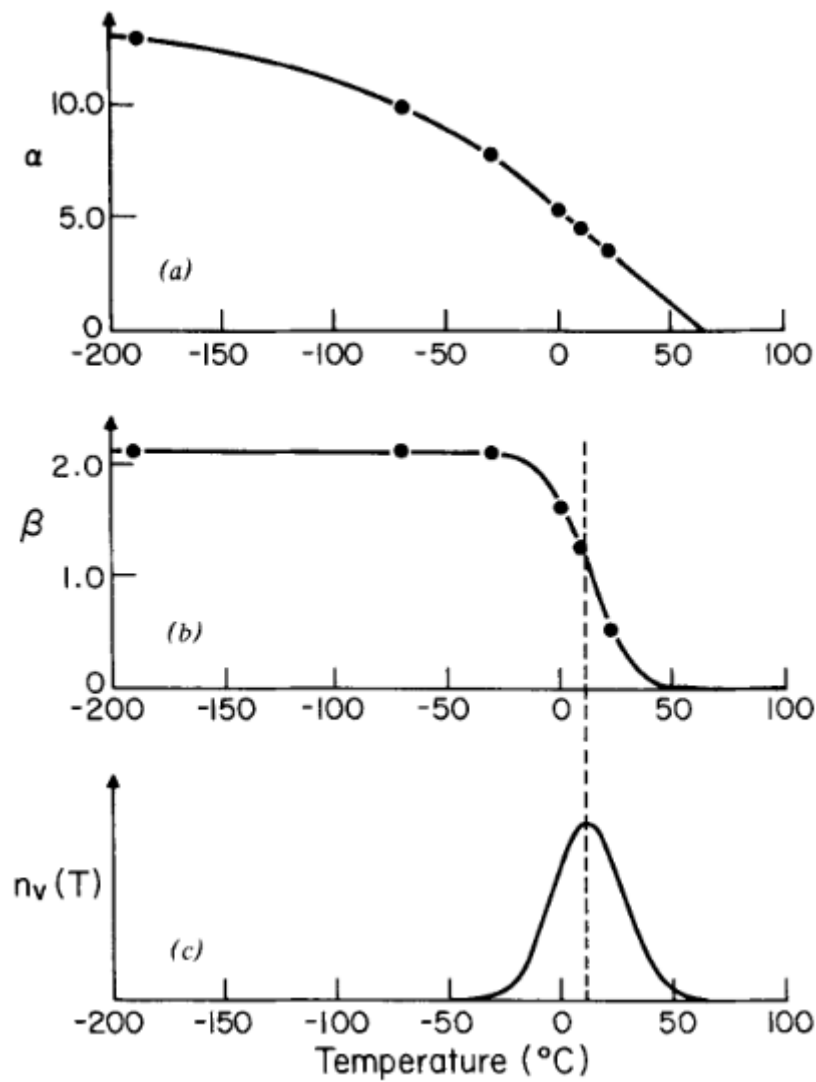


Figure 3.13 Kinetic parameter α & β vs. Temperature reported by Cohen^[47].

From the Fig.3.13 we can observed the reversed correlation between temperature and value of α/β . The prior reason of increasing volume of α' at low strain level is attribute to increasing number of intersections. This can be detailly explained through the adiabatic deformation. Adiabatic deformation may be induced at the zone of intense shear deformation, which is phenomenon represent the extremely fast rate of heat generation in system. As the heat generation rate at shear localization area considerably higher than its surroundings, which cause the significant temperature rise in shear band^[22].

As shown in Fig.3.12, the increasing temperature rise is corresponding to increasing displacement. Given by Angel's data, value of α and β are reversely correlated to temperature. Therefore, in aspect of large displacement, with high rate, there is insufficient time for the heat dissipation, which gives a rise to drastic increase in temperature, resulting in less embryos and intersections and decreasing value of α and β . In contrast, at slow rate, the time suffices for the heat dissipation, which cause mild temperature rise. Besides, at slow rate, growth of α' fostered by repeated nucleation and coalescences. As the proceeding of coalescences, α' grows into lath-like and polyhedral structures.

On other hand, in respect of small displacement, high strain rate accounts for the large amount of shear bands. There is mild temperature rise at low strain level, contributes to a less decreasing value of α and β . In consequence, there is larger volume fraction of α' .

However, these relations can't be applied to our case simply because of absence of ε martensite and shear band intersection. Therefore, the strain rate effect on martensitic transformation associates with another aspect, critical stress for phase transition and yield stress. The relation between strain rate and yield stress can be represented by the following equation^[65]:

$$\sigma_y = \sigma_{y0} + c \cdot \dot{\varepsilon}^m$$

$$c, m = \text{constant}$$

$$\sigma_{y0} = \text{reference static yield stress level}$$

$$\sigma_y = \text{dynamic yield stress level}$$

$$m = \text{strain rate sensitivity}$$

As the strain rate increases, the yield stress will correspondingly rise. This can be attributed to drastic rising density of dislocation under high strain rate, which enhance the strength. Base on previous result, yield stress for static and dynamic compression is 850 and 1270MPa respectively. Therefore, the critical stress value for martensitic transformation may locate between 850 to 1270MPa.

3.5.2 Morphology of deformation induced martensite

In both athermal induced martensitic transformation and deformation induced martensitic transformation, thin-plate martensite can nuclei at plane paralleled to $\{111\}_\gamma$ plane. Fig.3.14 shows the appearance of α' martensite phase in a shape of thin plate with large area. The morphology mechanism of α' is very complicated which is strongly dependent on M_s temperature and aging treatment.

Varied shapes of martensite are corresponding to different morphology and crystallography. Thin-plate martensite usually acquires lowest M_s and lath-like martensite has highest M_s temperature. It is reported by Maki^[58] that, as the temperature further decrease of M_s , the substructure of martensite will be converted from dislocations to twins. The morphology of martensite and its corresponding substructure are listed in Table 3.3.



Table 3.3 Morphology of martensite and their corresponding M_s temperature and substructure

	Morphology	Substructure	H.P.	O.R.*	M_s	Alloy
1	Lath	Dislocations	(111) _A or (557) _A	K-S	High ↑ ↓ Low	
2	Butterfly	Dislocations + Twins	(225) _A	K-S		Fe-Ni-(C) Fe-Ni-Cr-(C)
3	(225) type plate	Dislocations + Twins	(225) _A	K-S		Fe-7Cr-1C Fe-5Mn-1C Fe-3Mn-3Cr-1C
4	Lenticular	Dislocations + Twins (Mid-rib)	(259) _A or (3 10 15) _A	N G-T		
5	Thin-plate	Twins	(3 10 15) _A	G-T		Fe-high Ni-C Fe-7Al-2C Fe-25at%Pt Fe-Ni-Co-Ti

* K-S: Kurdjumov-Sachs relationship, N: Nishiyama relationship
G-T: Greninger-Troiano relationship

There is no obvious twinning under EBSD in Fig.3.14 and Fig.3.16, which attribute to high stacking fault energy of NCATB HEA. H/L ratio is applied to

describe morphology of thin-plate martensite, where H and L indicate plate width and plate length respectively. It is reported by Li^[49] that as the H/L increases, the lenticular martensite will appear. This results from the conversion from thin-plate martensite to coupled-plate to lenticular martensite.

- FCC (austenite) Fe 
- BCC(martensite)Fe 

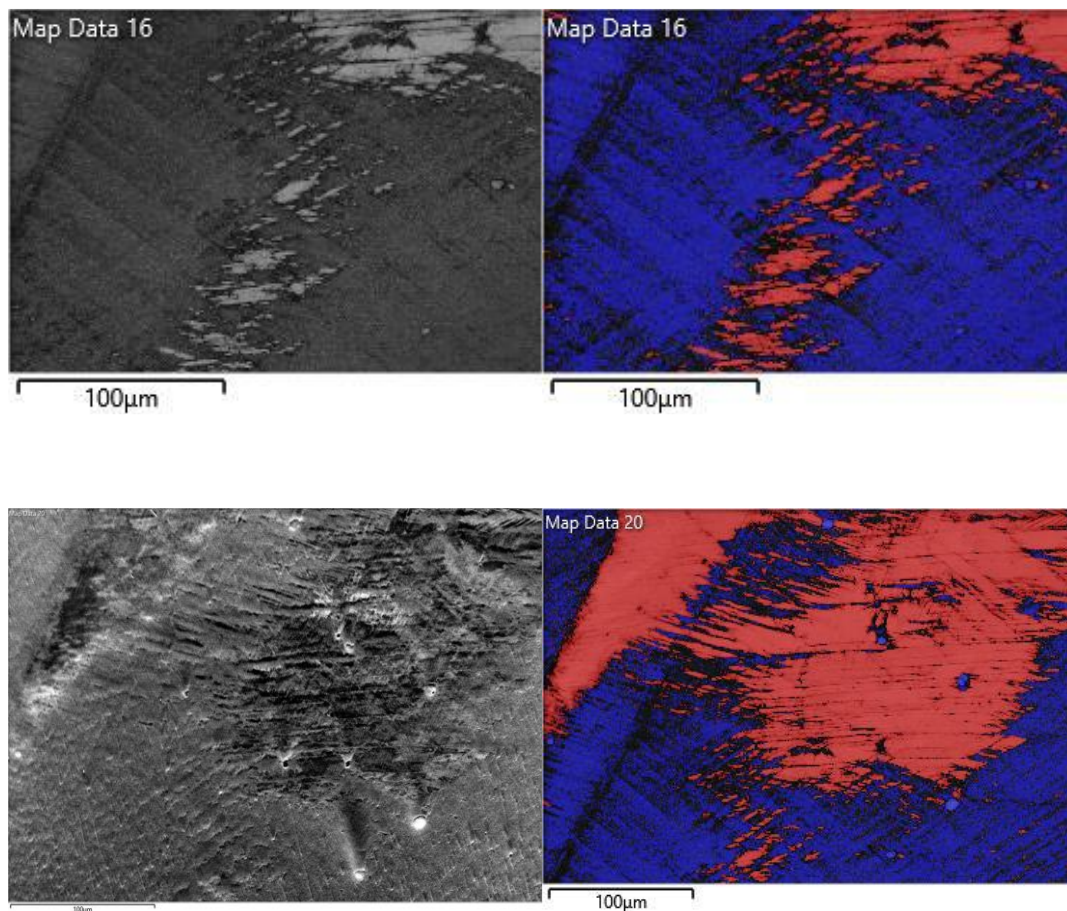


Figure 3.14 Mixture of FCC matrix and deformation induced martensite.

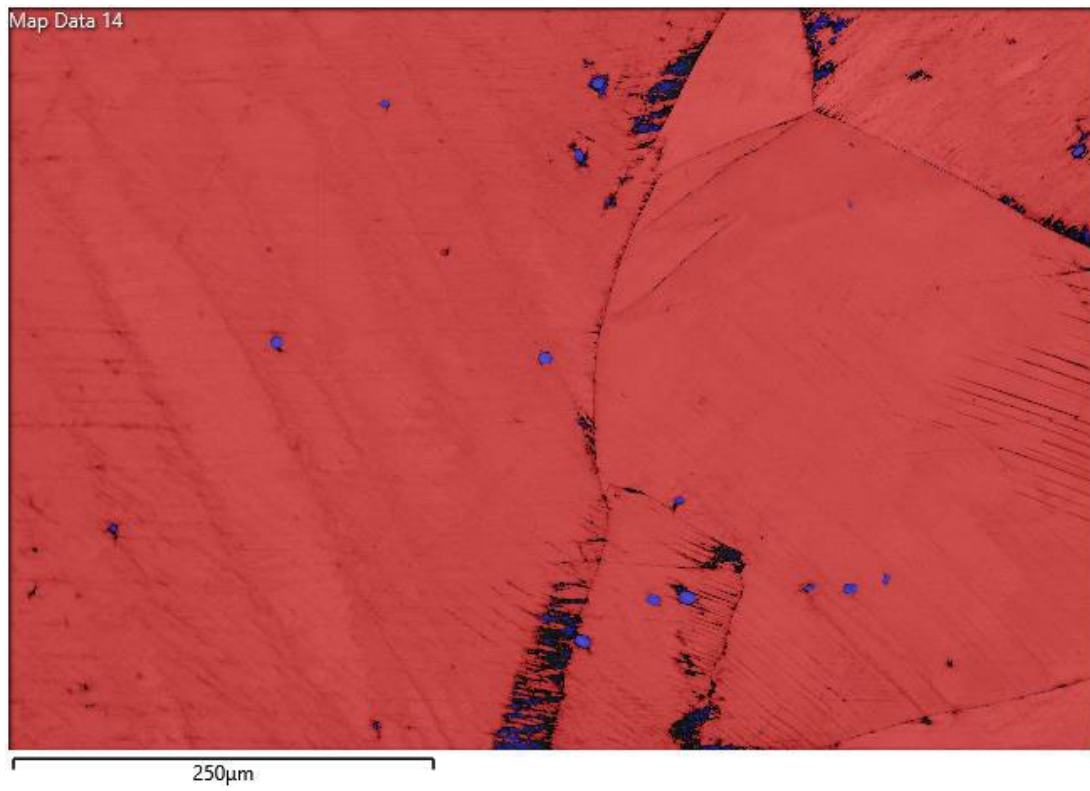
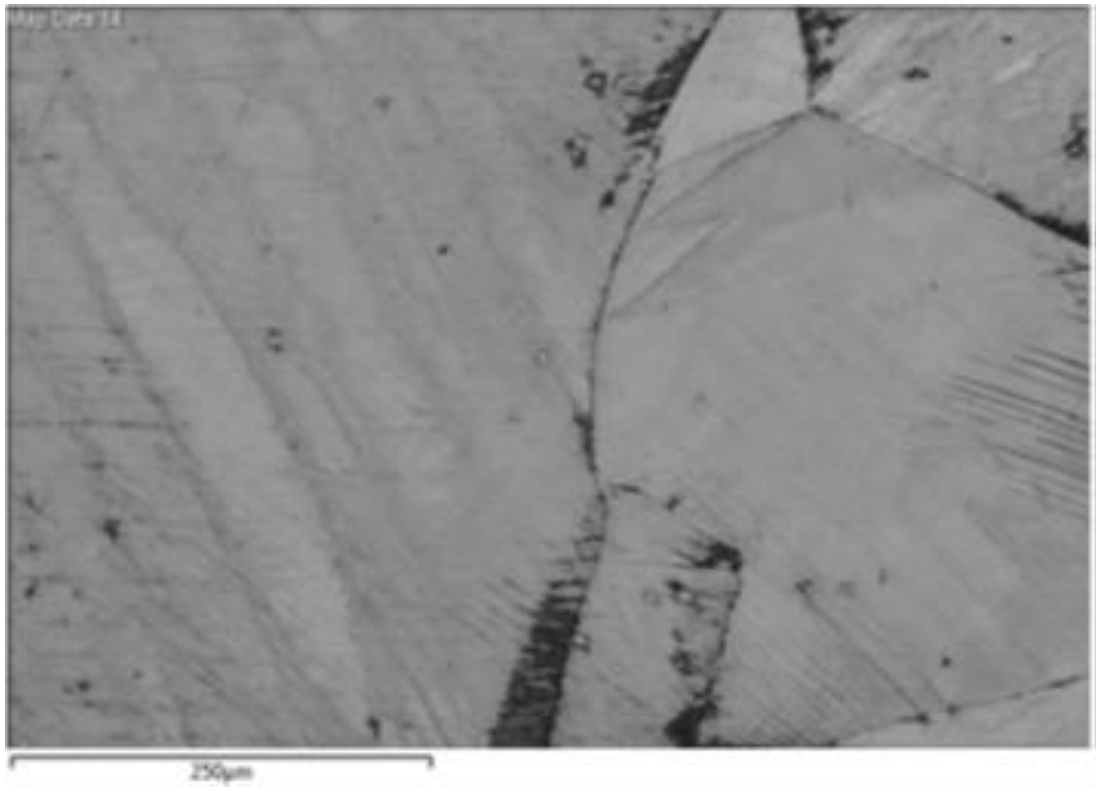


Figure 3.15 EBSD band contrast (BC) map.

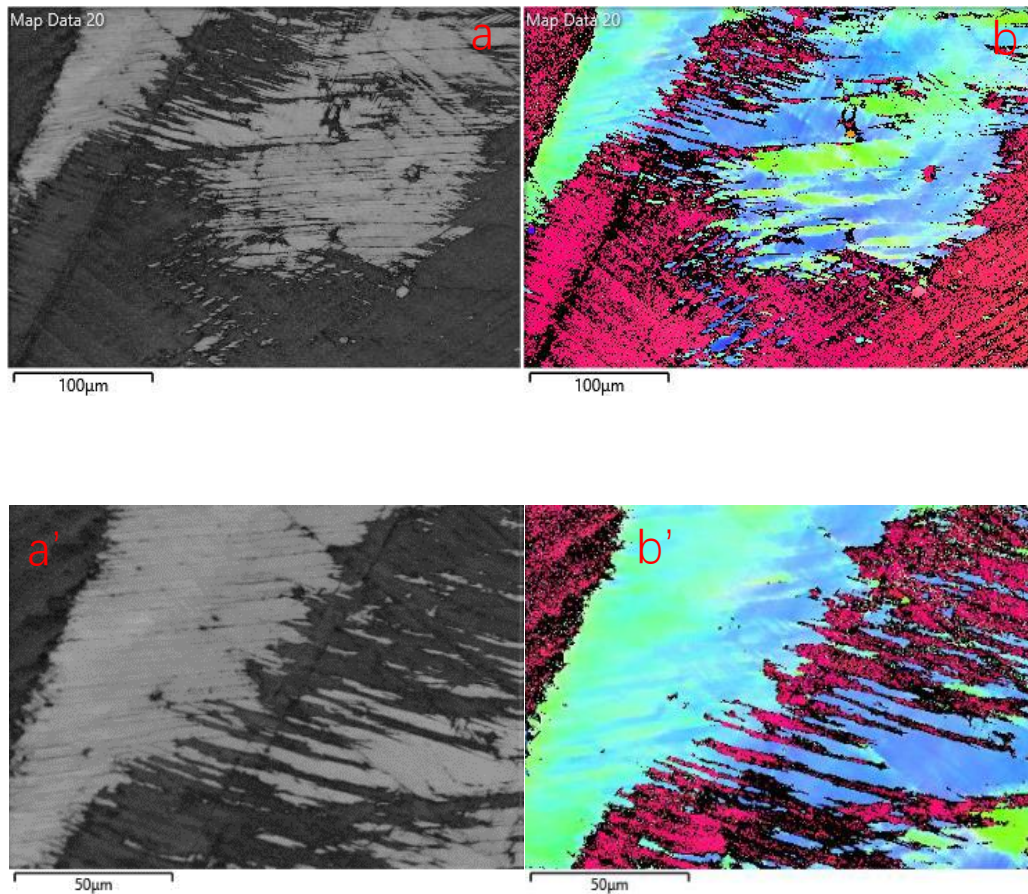


Figure 3.16 EBSD BC map (a & a') and EBSD IPFX map (b & b') of deformation induced martensite with different orientation.

Other than the aspect of nucleation mechanism, the critical factor to dictate morphology of martensite in NCATB HRA is $\gamma' - Ni_3Al$ and addition of certain element. Based on the prior present theory, higher M_s temperature will propel the formation of lath-like and lenticular martensite, meanwhile, establishment of M_s are depending on aging time. Different morphology of martensite and their corresponding solutes size and aging time were shown in Fig.3.17. Besides, the reason behind influence made by aging time is the stability of matrix phase. With rising aging time over 24h under $700^\circ C$, coherency between $\gamma' - Ni_3Al$ and γ matrix will no longer exist, M_s will prominently increase. Considering the sample

was aged under 600°C and 24h, coherency is maintained which support thin-plate to commence.

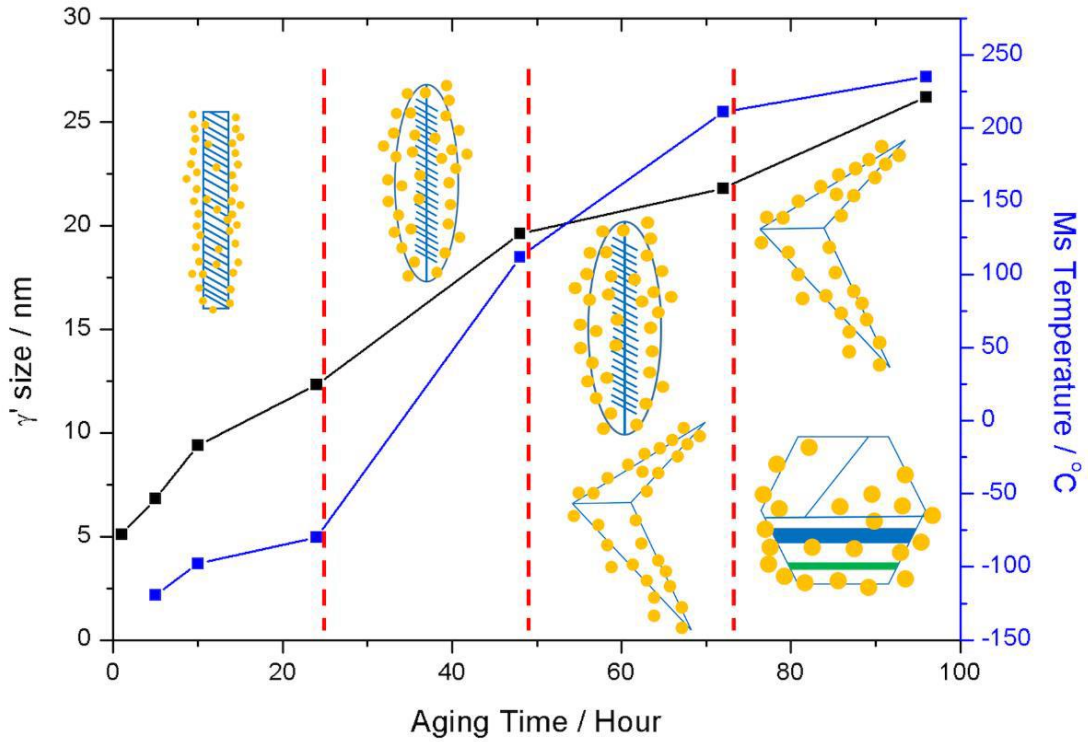


Figure 3.17 Configuration of martensite morphology under different aging time (700°C)

3.5.3 Nucleation of α' martensite

The mechanism of deformation induced martensitic transformation was first proposed by Cohen and Olson^[20]. They carried out a theory that the nucleation of α' is strongly depending on its major precursor ϵ -HCP martensite, which can be expressed in relation below:

$$\frac{dN_{\alpha'}}{dt} = p \frac{dN_{\epsilon}}{dt}$$

where $N_{\alpha'}$ and N_{ϵ} are nucleation rate of α' and ϵ respectively. ϵ martensite plays an important role as lowering the driving force energy to form α' . Moreover, they claimed that α' can only nuclei at the overlapping site of ϵ bands.

The nucleation of ε and α' martensite follows certain orientation relationship with γ matrix phase, while ε abides by Shoji-Nishiyama orientation relation: $\{111\}_\gamma // \{0001\}_\varepsilon$ and α' abides by Kurdjumov orientation relation: $\{111\}_\gamma // \{011\}_{\alpha'}$. Moreover, other than at sites of ε bands or shear bands intersection, α' is found that can form in a individual ε band if stability of matrix phase is low enough. Whereas, the formation of ε phase is closely related to the stacking fault energy due to its similar nucleating mechanism with mechanical twinning. The formation mechanism of ε and mechanical twinning can be distinguished through required energy to overcome. The formation of twinning demands presence of partial dislocation on successive $(111)_\gamma$ plane. Whereas, in respect of ε martensite, which requires occurrence of Shockley partial dislocation with burgers vector of $\frac{1}{6}[11\bar{2}]$ on adjoining $(111)_\gamma$ plane. Due to higher repulsive force between dislocation is higher in twinning, twinning is expected to be less favorable to form comparing to ε martensite. In general, materials with high stacking fault energy will not only suppress the formation of twinning but also ε martensite and replace them with high density of dislocation. Therefore, the nucleation of α' without forming of ε in high stacking fault energy is in conflict with the theory developed by Cohen. It is proposed by Breedis and Kaufman^[51] that the nucleation of α' can be independent from the occurrence of ε bands. Formation of ε bands is corresponding to stability of γ matrix phase. The reason why there is no ε martensite being observed in EBSD and TEM can be explained in respect of required free energy for phase transition. The relatively high atomic ratio of Ni (28.5%) in

NCATB HEA greatly enhance the stability of γ austenite phase which higher the stacking fault energy and lower the M_s temperature. When sufficient Ni is added to matrix, chemical driving force required to propel formation of $\varepsilon - \Delta G_{RT}^{fcc \rightarrow hcp}$ surpass that for $\alpha' - \Delta G_{RT}^{fcc \rightarrow bcc}$, which subsequently leads to γ to α' martensitic transformation in NCATB HEA. The nucleation of BCC α' martensite is also confirmed through HRTEM (high resolution transmission electron scope) which is shown in Fig.3.18. In Fig.3.18 (b), it shows the different orientation of crystal, which is caused by martensitic transformation. In the FCC shown in Fig.3.18(c), the FFT patterns shows the (211) and (011) family plane, besides, the $(011)_{\alpha'}$ is paralleled to $(11\bar{1})_{\gamma}$ which is followed by Kurdjumov-Sachs orientation.

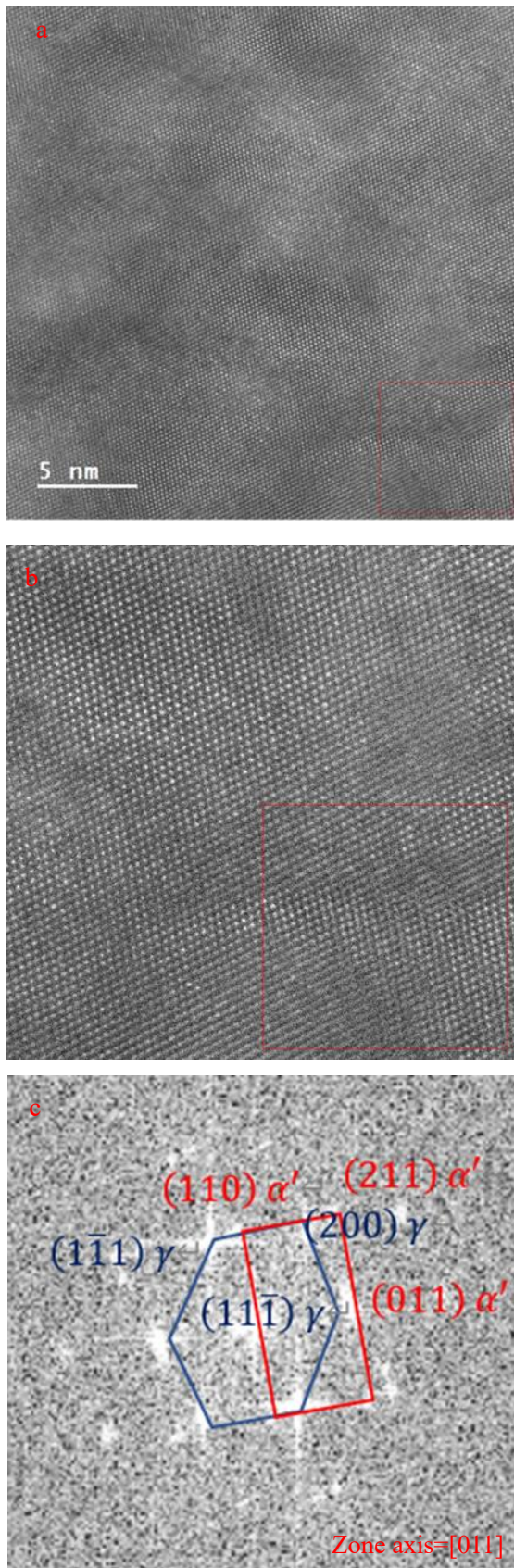


Figure 3.18 (a)(b) HRTEM BF (bright field) images of high strain rate deformed NCATB specimen (c) FFT pattern in selected area (red box)

3.5.4 Grain size effect on martensitic transformation

According to Fig.3.10, as aging time length increases, M_s and M_f temperature would correspondingly raise, this is related to the grain size effect more specifically grain size impact on stacking fault energy of matrix phase. Coarsening austenite matrix phase would lift up M_s temperature, while fined grain matrix phase can greatly lower M_s temperature. However, due to larger fraction of grain boundaries in refined grains, which contributes more of nucleation sites for martensite^[60]. On top of that, the growth of thin-plated martensite would be initialized at grain boundary due to lower required driving force, then it develop inward to the grains.

3.6 Failure under quasi-static compression test

The cylindrical sample reached its sudden failure point at around stress equals to 2.7GPa and a relatively small strain equals to 0.2, which indicts a less desired ductility comparing with traditional HEAs such as Cantor alloy. The occurrence of failure behavior at relatively small strain level may associates with the grain precipitation of NiAl- β phase, which contributes to higher brittleness.

Through EDX scanning result shown in Fig.3.18 and Fig.3.19 we can observe there is uneven Al distribution of Al at certain area at fracture surface. However, this result may not be very accurate, since the grain boundary cannot be observed.

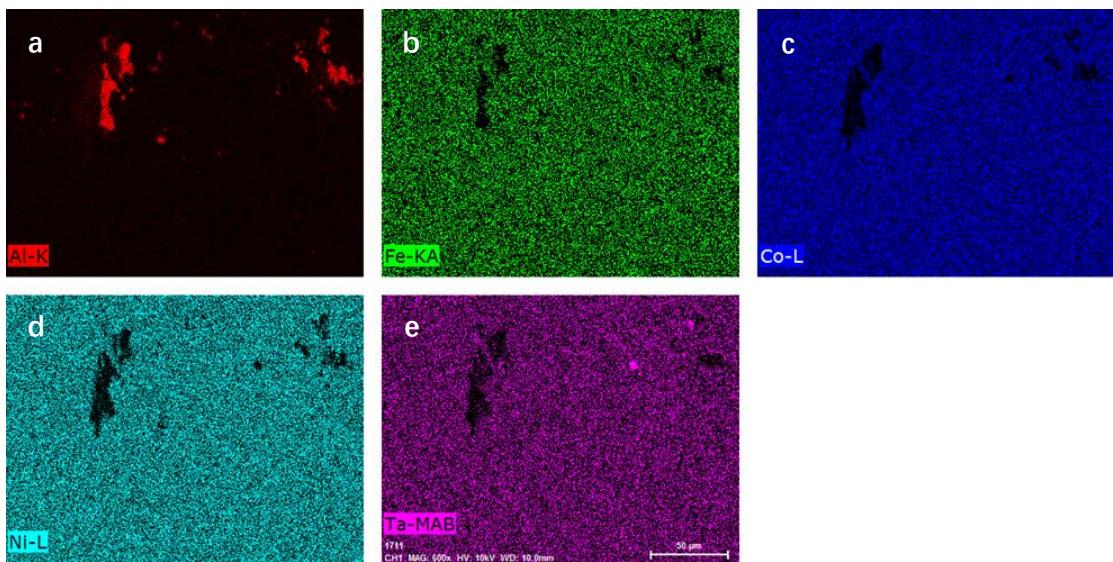
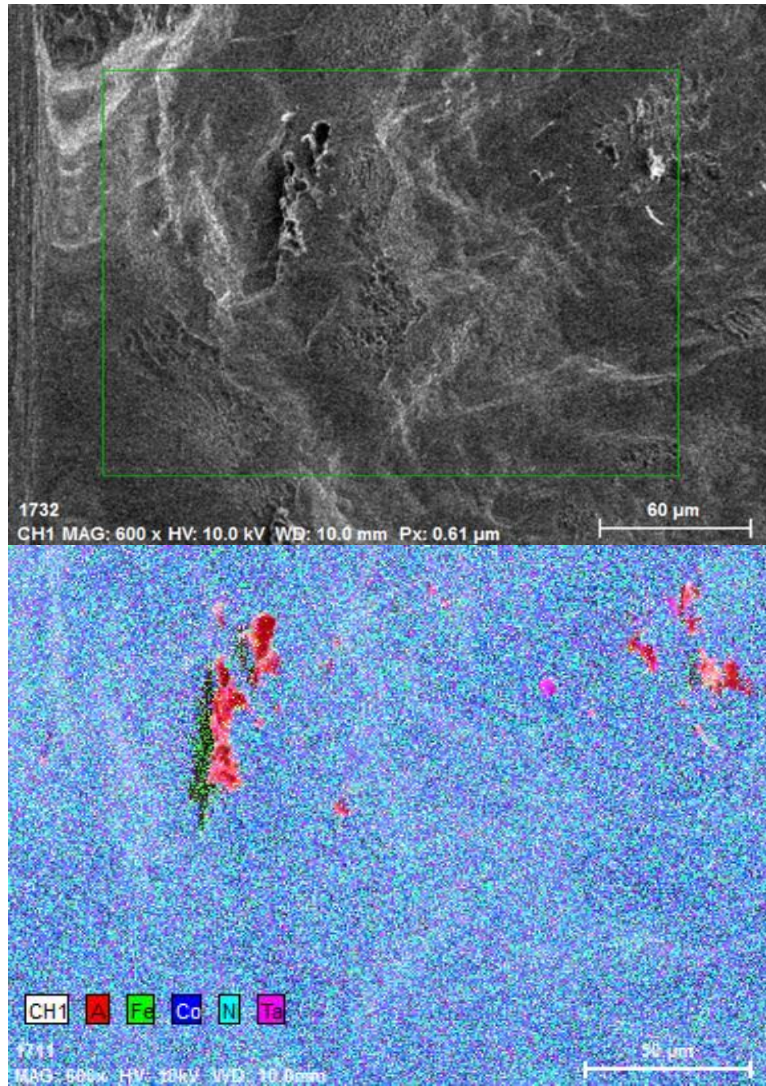


Figure 3.19 EDX mapping for cracking area. Element distribution of: (a)Al (b)Fe (c)Co (d)Ni

(e)Ta

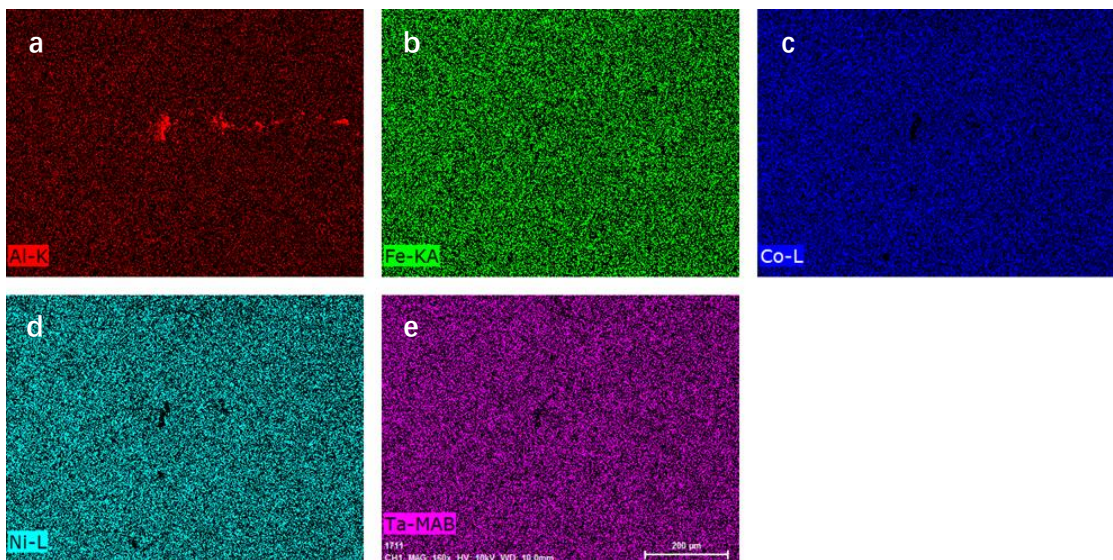
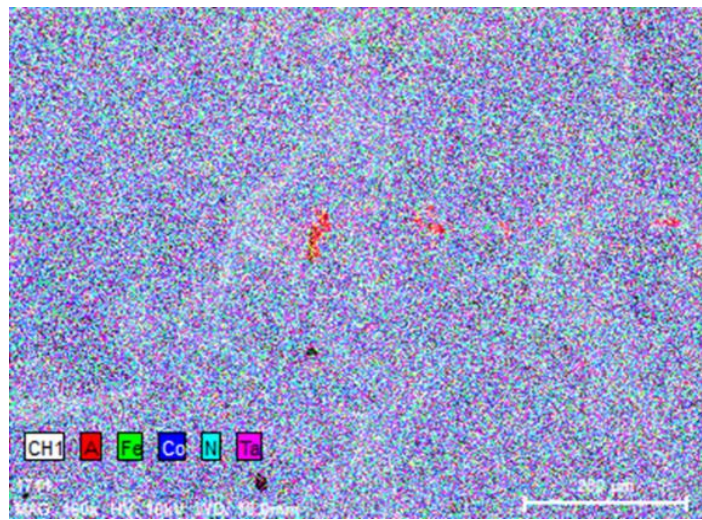
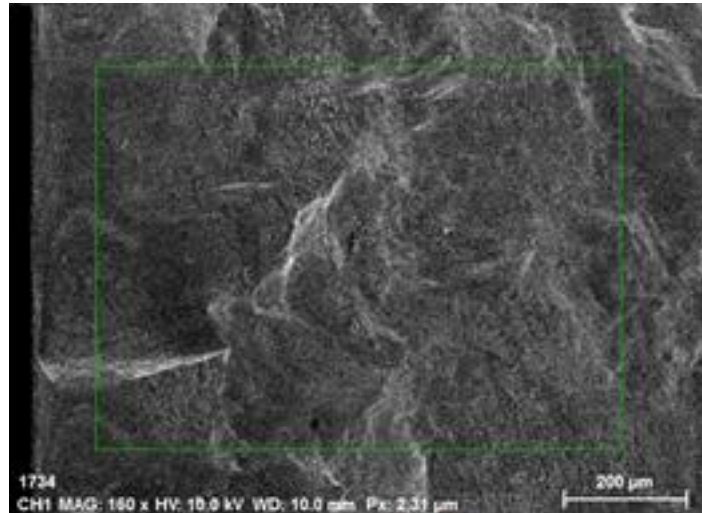


Figure 3.20 EDX mapping for cracking area. Element distribution of: (a)Al (b)Fe (c)Co (d)Ni

(e)Ta

3.7 $\beta - NiAl$ Grain boundary precipitates

Precipitation of $\beta - NiAl$ is more often to present at high-angle boundaries due to its energetically favorability. As the volume fraction of $\beta - NiAl$ increases, which can significantly weaken the ductility of materials which accounts for the relatively small strain level at failure in quasi-static compression test. The forming mechanism of $\beta - NiAl$ precipitates is correlated to Ta. Given that B-Ta compound has a super low mixing enthalpy which lead to formation of Ta_2B precipitates prior to that of $\beta - NiAl$. It is shown in the Fig.3.21 that, grain boundary marked with red line has high grain boundary angle has more of grain boundary precipitates along grain boundary with relatively high angle. The $\beta - NiAl$ tends to form at sites where Ta exist. However, with addition of B, which leads to occurrence of Ta_2B compounds. The lattice structure of Ta_2B is attribute to tetragonal structure with $a_0=0.5778nm$ ^[55]. Precisely because of the lattice mismatch between Ta_2B and $\beta - NiAl$ (0.288nm and 0.5778nm), formation of the latter one is suppressed. Although we can not confirm the presence of Ta_2B , it's considered to be inhibitor of $\beta - NiAl$ precipitates. With the suppression of grain boundary precipitates, the ductility would be optimized with better ductility. As shown in Fig.3.20, prominent grain boundary precipitates are found along grain boundary represented with green and red lines. More prominent feature of precipitated were discovered along red lines, which can be explained by higher angle of grain boundary comparing to the green one. More specific theory of grain precipitates along high angle and low angle grain boundaries is developed by Zhang^[55] and shown in Fig.3.22. Grain boundary precipitates is also

able to affect martensitic transformation. Due to lower energy barrier for phase transition along grain boundaries, it provides nucleation sites of α' at the preliminary stage of martensitic transformation. However, due to coarse grains of the specimen, the volume fraction of grain boundary is small, which severely takes away nucleation sites for $\beta - NiAl$ precipitates. Therefore, although there is grain boundary precipitates, their effect on the mechanical properties and martensitic transformation is mild. On top of that, other than SEM, more accurate analysis is hard to apply to. The Ta_2B is very difficult to characterize due to low energy of B.

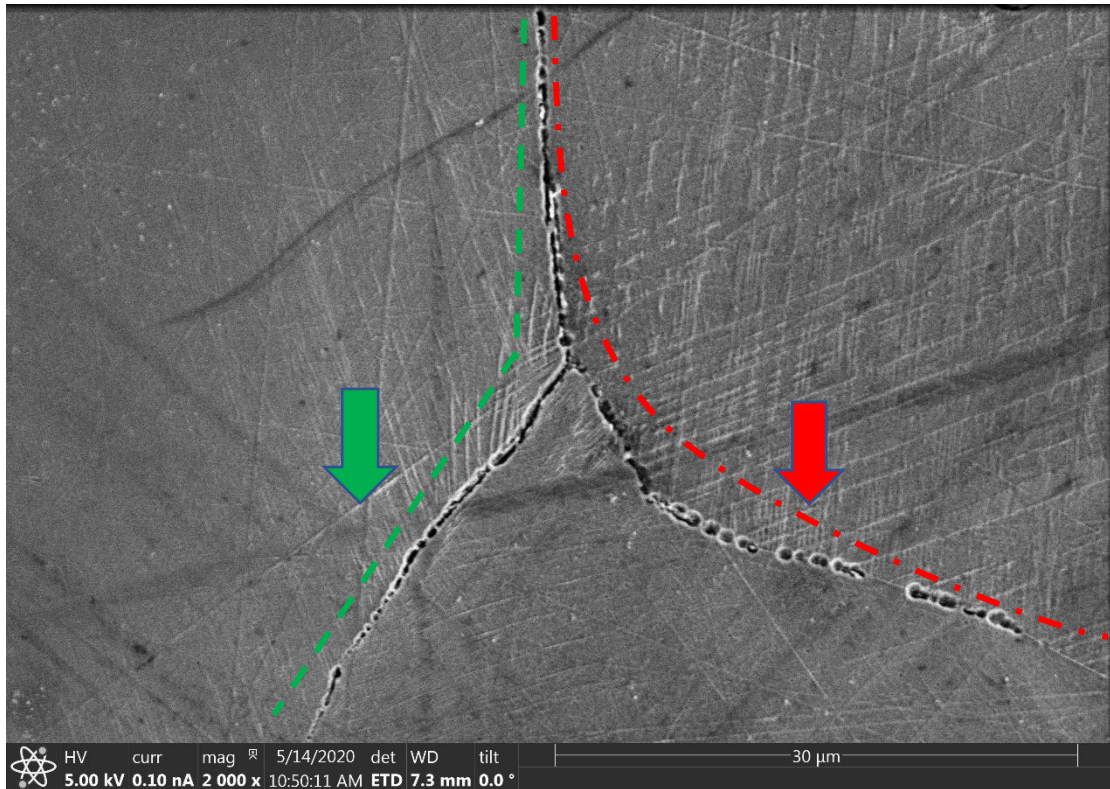


Figure 3.21 Image of triple point junction grain boundary.



Figure 3.22 Grain boundary precipitates in deformed hat shape specimen after etching.

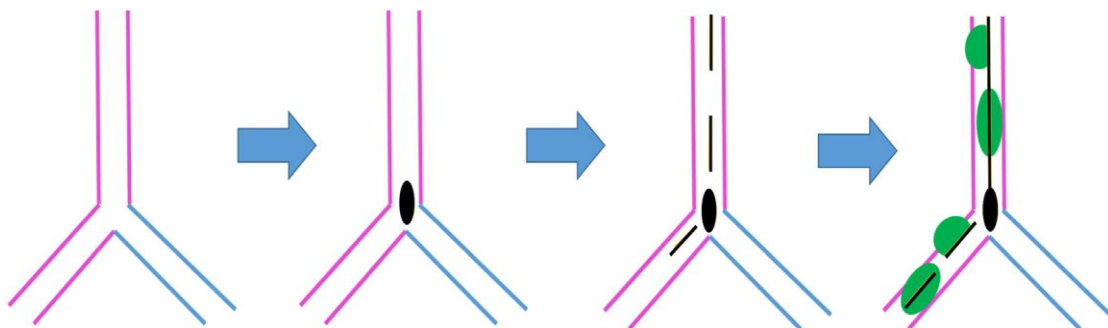


Figure 3.23 Configuration of formation of Ta and NiAl- β precipitates at grain boundaries, Pink line is high-angle boundaries ($>15^\circ$), blue line is low angle boundary ($<15^\circ$)^[55].

3.8 Microband

As we see in the SEM image of specimen surface (Fig.3.23), we have noticed the band structure developed next to the crack due to compression. Further verification and analysis were done through TEM and EBSD. As we see in Fig.3.24, the crystalline structure remains similar in band structure which is FCC

austenite. However, considerable amount of α' martensite which is represented in yellow color in Fig.3.25 is discovered surrounding microbands, which may lead to assumption that microband could foster the nucleation of α' martensite in NCATB HEA. Since microband shares similar feature with twinning, which blocks and hinders the migration of dislocation. The commence of α' surrounding microband could be explained by the localized stress and back stress generated by microband formation at those areas. As the stress localization further developed, the critical stress for martensitic transformation is met, which support α' formation. From Fig.3.25, the length of shear band (in green) can reach over $200\mu m$ which is attributed to sufficient growing spacing provided by coarse grains ($>200\mu m$). The crystalline structure in microband remains unchanged as FCC austenite. The crystalline misorientation was analyzed through inverse pole figure along Y-axis (IPFY) in Fig.3.24, where we can obtain a roughly ten degrees of misorientation inside the microband. Other than the its possible effect on martensitic transformation, it can also strengthen the materials through generating high density of dislocation.

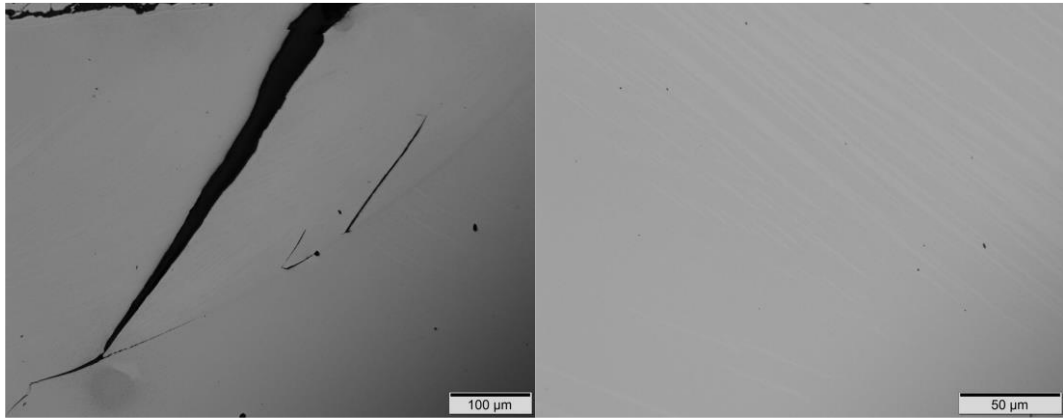


Figure 3.24 SEM image of microband

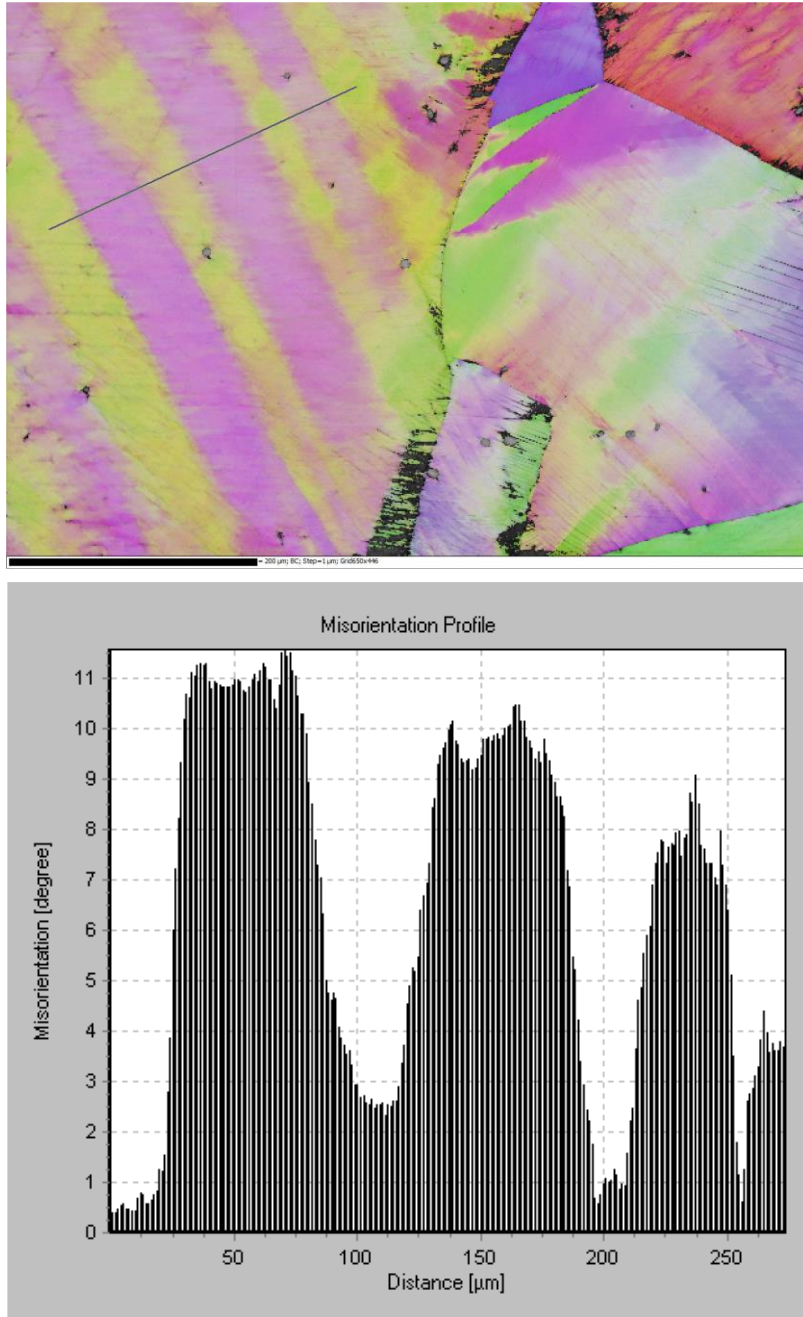


Figure 3.25 IPFY images and its corresponding misorientation profile of microband

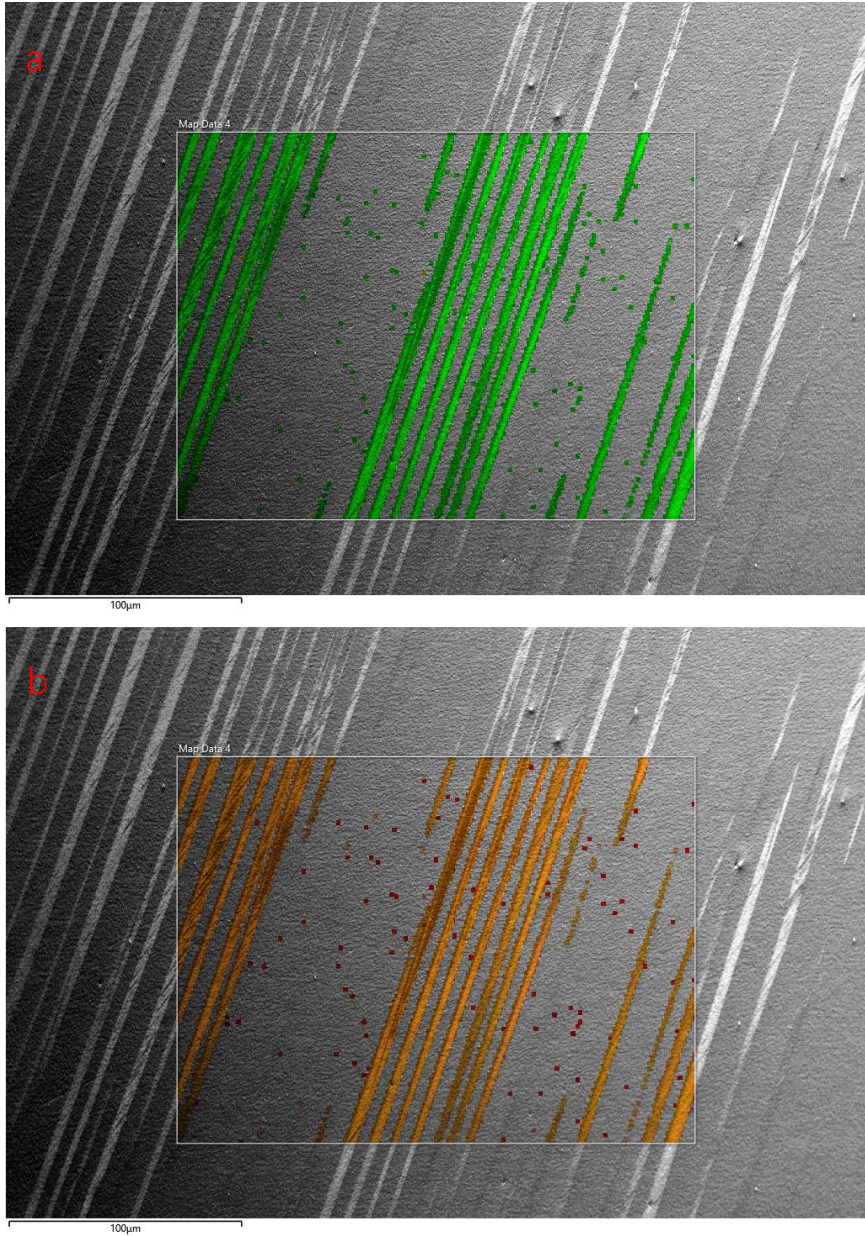


Figure 3.26 (a) EBSD phase map of microbands (b) IPFZ (inverse pole figure) map of microband

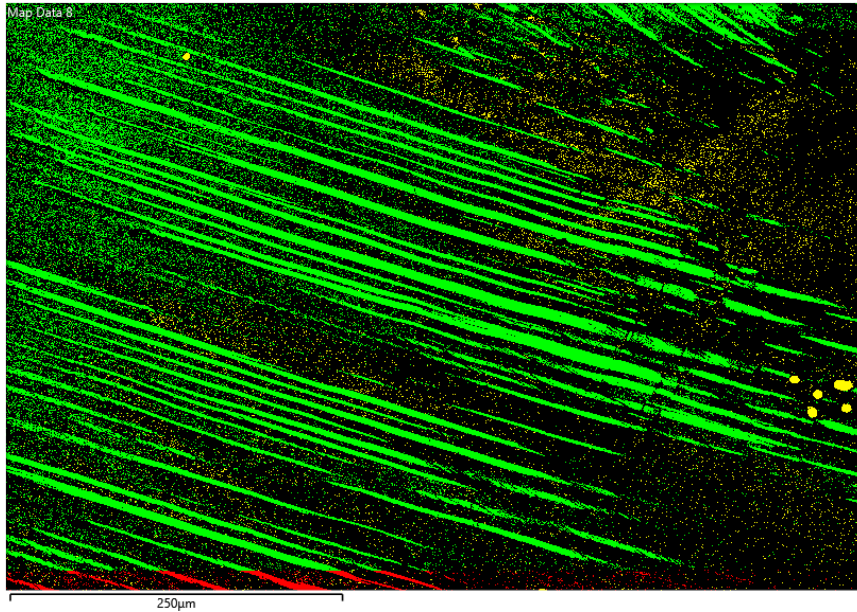


Figure 3.27 EBSD phase map of microband(green) and surrounding martensite(yellow)

4. Conclusion

- (1) There is martensitic transformation occurs in NCATB HEA, more specifically, $\gamma \rightarrow \alpha'$ transformation. This phenomenon associates with high strain rate with relatively small strain level.
- (2) During the compression, there is no sign of formation of ϵ martensite. Higher stability of matrix phase contributes a higher stacking fault energy which causes the absence of ϵ martensite. At small strain level, high strain rate would be beneficial to nucleation of α' .
- (3) Under high strain rate, material behaves with higher yield stress which make it available to surpass the critical for phase transformation. This associates with the strain rate effect on martensitic transformation of NCATB HEA.
- (4) The precipitate mechanism of NCATB HEA is strongly dependent on the addition of different chemical component. The solid solution phase $\text{NiAl}_3\text{-}\gamma'$ is a coherent

phase with matrix austenite phase when precipitate size is under critical value. The size of precipitates under 600°C/24h is significantly lower than its critical value which maintains phase coherency. It strengthens the material through increasing required drive force to move dislocation.

(5) Grain boundaries precipitates $\beta - NiAl$ is observed in NCATB HEA, whose formation can be suppressed by the addition of B.

(6) Microbands were observed in specimen. α' martensite seems more favorable to form around microbands.

5. Future plan

This thesis describes the mechanical properties and their corresponding mechanism of NCATB HEA at dynamic compression test and quasi-static compression test. In order to obtain a more accurate and overall understanding of strain rate effect on martensitic transformation and how microbands affect phase transformation, some future work can be carried out.

- (1) More dynamic compression test with various applied strain rate. Analyze the strain rate effect on martensitic transformation.
- (2) Applying dynamic compression test under different temperature (low, room, high temperature).
- (3) Estimation of stacking fault energy of NCATB HEA through TEM analysis. Verify high stacking fault energy feature suppresses formation of ϵ martensite and twinning through observing Shockley partial dislocation under TEM.
- (4) Understand strengthening and plasticity mechanism of NCATB HEA.

6. References

- [1]. Ahlers, M. (2004). The martensitic transformation. *Revista Materia*, 9(3), 169-183.

- [2]. Fu, H., Zhao, H., Zhang, Y., & Xie, J. (2017). Enhancement of superelasticity in Fe-Ni-Co-based shape memory alloys by microstructure and texture control. *Procedia engineering*, 207, 1505-1510.

- [3]. Danilhenko, V. E. (2017). Nanostructurization of Fe-Ni Alloy. *Nanoscale research letters*, 12(1), 201.

- [4]. Liang, Z., Zhao, Q., Singh, P. M., Wang, Y., Li, Y., & Wang, Y. (2015). Field studies of steam oxidation behavior of austenitic heat-resistant steel 10Cr18Ni9Cu3NbN. *Engineering Failure Analysis*, 53, 132-137.

- [5]. Handoko, W., Pahlevani, F., Hossain, R., & Sahajwalla, V. (2019). Stress-induced phase transformation and its correlation with corrosion properties of dual-phase high carbon steel. *Journal of Manufacturing and Materials Processing*, 3(3), 55.

- [6]. Borovikov, V., Mendeleev, M. I., King, A. H., & LeSar, R. (2015). Effect of stacking fault energy on mechanism of plastic deformation in nanotwinned FCC metals. *Modelling and Simulation in Materials Science and Engineering*, 23(5), 055003.

- [7]. Koshelev, P. F. (1971). Mechanical properties of materials at low temperatures. *Strength of Materials*, 3(3), 286-291.

- [8]. George, E. P., Curtin, W. A., & Tasan, C. C. (2020). High entropy alloys: A focused review of mechanical properties and deformation mechanisms. *Acta Materialia*, 188, 435-474.

- [9]. Patriarca, L., Ojha, A., Sehitoglu, H., & Chumlyakov, Y. I. (2016). Slip nucleation in single crystal FeNiCoCrMn high entropy alloy. *Scripta Materialia*, 112, 54-57.
- [10]. Laplanche G, Bonneville J, Varvenne C, Curtin W, George EP. Thermal activation parameters of plastic flow reveal deformation mechanisms in the CrMnFeCoNi high-entropy alloy. *Acta Materialia* 2018;143:257–64.
- [11]. Leyson, G. P. M., Hector Jr, L. G., & Curtin, W. A. (2012). First-principles prediction of yield stress for basal slip in Mg–Al alloys. *Acta materialia*, 60(13-14), 5197-5203.
- [12]. Petch, N. J. (1953). The cleavage strength of polycrystals. *Journal of the Iron and Steel Institute*, 174, 25-28.
- [13]. Marc André Meyers, Krishan Kumar Chawla - *Mechanical Behavior of Materials*-Cambridge University Press (2008)
- [14]. Conrad, H., & Narayan, J. (2000). On the grain size softening in nanocrystalline materials. *Scripta materialia*, 42(11), 1025-1030.
- [15]. Rahman, K. M., Vorontsov, V. A., & Dye, D. (2015). The effect of grain size on the twin initiation stress in a TWIP steel. *Acta Materialia*, 89, 247-257.
- [16]. Romanov, A., Vladimirov, V. I., & Nabarro, F. R. N. (1992). Disclinations in Crystalline Solids, in *Dislocations in Solids*.
- [17]. Sidhoum, Z., Ferhoum, R., Almansba, M., Bensaada, R., Habak, M., & Aberkane, M. (2018). Experimental and numerical study of the mechanical behavior and kinetics of the martensitic transformation in 304L TRIP steel: applied to folding. *The International Journal of Advanced Manufacturing Technology*, 97(5-8), 2757-2765.

- [18]. Galindo-Nava, E. I., & Rivera-Díaz-del-Castillo, P. E. J. (2017). Understanding martensite and twin formation in austenitic steels: A model describing TRIP and TWIP effects. *Acta Materialia*, 128, 120-134.
- [19]. Hauser, M., Wendler, M., Mola, J., Fabrichnaya, O., Volkova, O., & Weiß, A. (2020). Thermodynamic-Mechanical Modeling of Metastable High Alloy Austenitic CrMnNi Steels. In *Austenitic TRIP/TWIP Steels and Steel-Zirconia Composites* (pp. 651-678). Springer, Cham.
- [20]. Murr, L. E. (1981). *Shock Waves and High-Strain-Rate Phenomena in Metals*. Edited by Meyer MA and Murr LE, Plenum, NY, 607.
- [21]. Olson, G. B., & Cohen, M. (1972). A mechanism for the strain-induced nucleation of martensitic transformations. *Journal of the Less Common Metals*, 28(1), 107-118.
- [22]. Angel, T. (1954). Formation of martensite in austenitic stainless steels. *J. Iron Steel Inst.*, 177, 165-174.
- [23]. Timothy, S. P. (1987). The structure of adiabatic shear bands in metals: a critical review. *Acta Metallurgica*, 35(2), 301-306.
- [24]. Lindholm, U. S., & Yeakley, L. M. (1968). High strain-rate testing: tension and compression. *Experimental Mechanics*, 8(1), 1-9.
- [25]. Sharma, S., Chavan, V. M., Agrawal, R. G., Patel, R. J., Kapoor, R., & Chakravartty, J. K. (2011). Split-Hopkinson pressure bar: an experimental technique for high strain rate tests (No. BARC--2011/E/013). Bhabha Atomic Research Centre.
- [26]. Cantor, B.; Chang, I.T.H.; Knight, P.; Vincent, A.J.B. Microstructure development in equiatomic multicomponent alloys. *Mater. Sci. Eng. A* 2004, 375, 213–218.

- [27]. Cantor, B. (2007). Stable and metastable multicomponent alloys. In *Annales de chimie (Paris. 1914)* (Vol. 32, No. 3, pp. 245-256).
- [28]. Yeh, J. W., Chen, Y. L., Lin, S. J., & Chen, S. K. (2007). High-entropy alloys—a new era of exploitation. In *Materials Science Forum* (Vol. 560, pp. 1-9). Trans Tech Publications Ltd.
- [29]. Ranganathan, S. (2003). Alloyed pleasures: multimetallic cocktails. *Current science*, 85(10), 1404-1406.
- [30]. Himuro, Y., Ikeda, O., Kainuma, R., & Ishida, K. (2001). Effect of ausaging on the morphology of martensite in an Fe-25% Ni-7.5% Si alloy. *Le Journal de Physique IV*, 11(PR8), Pr8-205.
- [31]. Zhang, C., Zhu, C., Shin, S., Casalena, L., & Vecchio, K. (2019). Grain boundary precipitation of tantalum and NiAl in superelastic FeNiCoAlTaB alloy. *Materials Science and Engineering: A*, 743, 372-381.
- [32]. Nishiyama, Z. (2012). *Martensitic transformation*. Elsevier.
- [33]. MITCHELL, T., NEFF, D., & TROIANO, A. (1969). The influence of temperature, transformation, and strain rate on the ductility properties of austenitic stainless steels (Temperature, transformation and strain rate effects on tensile ductility properties of stable and metastable compositions of austenitic stainless steels). *ASM TRANSACTIONS QUARTERLY*, 62, 858-868.
- [34]. Hecker, S. S., Stout, M. G., Staudhammer, K. P., & Smith, J. L. (1982). Effects of strain state and strain rate on deformation-induced transformation in 304 stainless steel: Part I. Magnetic measurements and mechanical behavior. *Metallurgical Transactions A*, 13(4), 619-626.
- [35]. Murr, L. E., Staudhammer, K. P., & Hecker, S. S. (1982). Effects of strain state and strain rate on deformation-induced transformation in 304 stainless steel: Part II. Microstructural study. *Metallurgical Transactions A*, 13(4), 627-635.

- [36]. Burke, J. E., & Turnbull, D. (1952). Recrystallization and grain growth. *Progress in metal physics*, 3, 220-292.
- [37]. Burke, J. E. (1949). Some factors affecting the rate of grain growth in metals. *Aime Trans*, 180, 73-91.
- [38]. Li, Z., Zhao, S., Ritchie, R. O., & Meyers, M. A. (2019). Mechanical properties of high-entropy alloys with emphasis on face-centered cubic alloys. *Progress in Materials Science*, 102, 296-345.
- [39]. N. I. Vazquez-Fernandez, G. C. Soares, J. L. Smith, J. D. Seidt, M. Isakov, A. Gilat, V. T. Kuokkala & M. Hokka. Adiabatic Heating of Austenitic Stainless Steels at Different Strain Rates. *J. dynamic behavior mater.* 5, 221–229 (2019).
- [40]. Dodd, B., & Bai, Y. (2014). *Introduction to Adiabatic Shear Localization: Revised*. World Scientific Publishing Company.
- [41]. Taylor, G. I., & Quinney, H. (1934). The latent energy remaining in a metal after cold working. *Proceedings of the Royal Society of London. Series A, Containing Papers of a Mathematical and Physical Character*, 143(849), 307-326.
- [42]. Zubelewicz, A. (2019). Century-long Taylor-Quinney interpretation of plasticity-induced heating reexamined. *Scientific reports*, 9(1), 1-7.
- [43]. Staker, M. R. (1981). The relation between adiabatic shear instability strain and material properties. *Acta Metallurgica*, 29(4), 683-689.
- [44]. Culver, R. S. (1973). *Metallurgical effects at high strain rates. Metallurgical Effects at High Strain Rates*, Plenum Press, New York, 519-523.
- [45]. Walley, S.M.. (2007). Shear Localization: A Historical Overview. *Metallurgical and Materials Transactions A: Physical Metallurgy and Materials Science*. 38. 2629-2654. 10.1007/s11661-007-9271-x.

- [46]. Johnson, G. R., Hoegfeldt, J. M., Lindholm, U. S., & Nagy, A. (1983). Response of various metals to large torsional strains over a large range of strain rates—Part 1: Ductile metals.
- [47]. Olson, G. B., & Cohen, M. (1975). Kinetics of strain-induced martensitic nucleation. *Metallurgical transactions A*, 6(4), 791.
- [48]. Adarsh, S. H., & Sampath, V. (2019). Influence of microstructure on mechanical and magnetic properties of an Fe-Ni-Co-Al-Ta-B shape memory alloy. *Materials Research Express*, 6(7), 075701.
- [49]. Li, D. F., Zhang, X. M., Gautier, E., & Zhang, J. S. (1998). Morphology transitions of deformation-induced thin-plate martensite in Fe–Ni–C alloys. *Acta materialia*, 46(13), 4827-4834.
- [50]. Zener, C., & Hollomon, J. H. (1944). Effect of strain rate upon plastic flow of steel. *Journal of Applied physics*, 15(1), 22-32.
- [51]. Breedis, J. F., & Kaufman, L. (1971). The formation of Hcp and Bcc phases in austenitic iron alloys. *Metallurgical Transactions*, 2(9), 2359-2371.
- [52]. Geng, Yonghong and Lee, Doyup and Xu, Xiao and Nagasako, Makoto and Jin, Mingjiang and Jin, Xuejun and Omori, Toshihiro and Kainuma, Ryosuke. Coherency of ordered γ' precipitates and thermoelastic martensitic transformation in FeNiCoAlTaB alloys. *Journal of Alloys and Compounds*, 628, 287-292 (2015).
- [53]. He, Q., & Yang, Y. (2018). On lattice distortion in high entropy alloys. *Frontiers in Materials*, 5, 42.
- [54]. Sakamoto, H. (2002). Distinction between thermal and stress-induced martensitic transformations and inhomogeneity in internal stress. *Materials Transactions*, 43(9), 2249-2255.

- [55]. Zhang, C., Zhu, C., Shin, S., Casalena, L., & Vecchio, K. (2019). Grain boundary precipitation of tantalum and NiAl in superelastic FeNiCoAlTaB alloy. *Materials Science and Engineering: A*, 743, 372-381.
- [56]. Zhang, C., Zhu, C., Harrington, T., Casalena, L., Wang, H., Shin, S., & Vecchio, K. S. (2019). Multifunctional Non-Equiatomic High Entropy Alloys with Superelastic, High Damping, and Excellent Cryogenic Properties. *Advanced Engineering Materials*, 21(1), 1800941.
- [57]. Fahr, D. (1971). Stress-and strain-induced formation of martensite and its effects on strength and ductility of metastable austenitic stainless steels. *Metallurgical Transactions*, 2(7), 1883-1892.
- [58]. Maki, T. (1990). Microstructure and mechanical behaviour of ferrous martensite. In *Materials Science Forum* (Vol. 56, pp. 157-168). Trans Tech Publications Ltd.
- [59]. Maki, T., Furutani, S., & Tamura, I. (1989). Shape memory effect related to thin plate martensite with large thermal hysteresis in ausaged Fe–Ni–Co–Ti alloy. *ISIJ International*, 29(5), 438-445.
- [60]. Celada-Casero, C., Sietsma, J., & Santofimia, M. J. (2019). The role of the austenite grain size in the martensitic transformation in low carbon steels. *Materials & Design*, 167, 107625.
- [61]. Zinnia, N. A., Quadir, M. Z., Munroe, P. R., & Ferry, M. (2014). Unusual crystallographic aspects of microband boundaries within $\{111\}<110>$ oriented grains in a cold rolled interstitial free steel. *ISIJ international*, 54(6), 1346-1352.
- [62]. Huang, J. C., & Gray III, G. T. (1989). Microband formation in shock-loaded and quasi-statically deformed metals. *Acta metall*, 37(12), 3335-3347.
- [63]. Jackson, P. J. (1983). The formation of microbands by cross-slips. *Scripta metallurgica*, 17(2), 199-202.

- [64]. Cai, W., Bulatov, V. V., Chang, J., Li, J., & Yip, S. (2004). Dislocation core effects on mobility. *Dislocations in solids*, 12, 1-80.
- [65]. Rao, N. N., Lohrmann, M., & Tall, L. (1966). Effect of strain rate on the yield stress of structural steels. *Journal of Materials*, 1(1), 241-262.
- [66]. Patel, J. R., & Cohen, M. (1953). Criterion for the action of applied stress in the martensitic transformation. *Acta metallurgica*, 1(5), 531-538.